



High-resolution mapping of pluvial flooding in ungauged agricultural catchments

Matthieu Herpoel¹, Pierre Baert¹, Charles Bielders², Gilles Swerts¹, Aurore Degré¹

¹ TERRA Teaching and Research Centre, Gembloux Agro-Bio Tech, University of Liège, Gembloux, 5030, Belgium

5 ² Earth and Life Institute – Environmental sciences, Université catholique de Louvain, Croix du Sud 2, bte2, Louvain-la-Neuve, 1348, Belgium

Correspondence to: Matthieu Herpoel (matthieu.herpoel@uliege.be)

Abstract. Accurate pluvial flood mapping in ungauged agricultural catchments is often constrained by a lack of calibration data. This study evaluates a parsimonious, high-resolution (1 m) distributed framework assessing peak discharge along concentrated flow paths, validated against 39 events in two nested experimental catchments (84 and 111 ha). The framework decouples the rainfall-runoff process to systematically compare adjusted SCS-CN formulations against two spatially explicit routing algorithms (SCS vs. SWRRB). Within this specific local context, findings demonstrate that the Jain initial abstraction method significantly reduces volumetric bias, with the distributed approach statistically outperforming lumped modelling. However, performance remains strictly regime-dependent, driven by rainfall intensity rather than total depth. This exposes the structural limits of static Curve Number (CN) parameterizations in capturing rapid Hortonian dynamics, causing the model to dampen minor events while amplifying high-intensity storms. Regarding hydraulic transfer, both routing strategies yield statistically equivalent performance (median KGE 0.40 vs. 0.37). Crucially, while the routing phase acts as a mechanical propagator of volumetric uncertainty, it consistently synchronizes the overall runoff window. Applied to 25- and 100-year design storms, this framework successfully identifies hydrodynamic attenuation and kinematic synchronization at confluences. Based on these empirical observations, we propose this approach as a transferable blueprint to pinpoint hydraulic hotspots and strategically allocate proactive mitigation measures in vulnerable, unmonitored regions.

1 Introduction

Recognized as a major hydrological hazard, pluvial flooding occurs when intense rainfall generates excessive surface runoff and rapid, localized water accumulation, distinguishing it from traditional riverine flooding. Pluvial flood exposure across Europe is immense; in England alone, roughly one million properties are at high risk of surface water flooding, triple the number exposed to traditional riverine and coastal hazards (Environment Agency, 2025). Intensified by climate change, these rapid pluvial floods constitute a growing natural threat. The devastating July 2021 floods in Western Europe starkly illustrate this amplification of extreme meteorological events. Within just three days (14–16 July), parts of the Belgian Vesdre basin received up to 290 mm of rain (Journée et al., 2023), representing nearly one-fifth of the regional annual average (Ercicum et al., 2018). Predicting such localized hazards remains a fundamental hydrological challenge, a difficulty further compounded



by a lack of reliable monitoring in small or agricultural catchments, where gauge data are typically absent (Blöschl et al., 2019). Furthermore, while remote sensing (e.g., Copernicus EMS) provides useful a posteriori validation of flooded areas (Munawar et al., 2022), proactive risk management requires comprehensive a priori hazard mapping across all potentially vulnerable sites, regardless of past events. While the European Floods Directive (2007/60/EC) mandates a precise
35 quantification of these risks, meeting this requirement remains a critical challenge in ungauged catchments, where discharge data are non-existent. Consequently, there is an urgent need to develop robust, parsimonious modelling tools capable of spatially estimating and quantifying pluvial flood risks in unmonitored agricultural landscapes.

To address the complexities of pluvial flood risk mapping, the scientific community has developed a spectrum of methodological approaches specifically tailored to surface runoff. In data-scarce agricultural catchments, alternative index-
40 based approaches have gained prominence; for instance, Kourgialas and Karatzas (2011), Kazakis *et al.* (2015), and Vojtek *et al.* (2019) developed multi-criteria susceptibility indices integrating static factors such as topography, land use, and geology. While operationally efficient for identifying potential hazard zones (Mudashiru et al., 2021), these heuristic methods remain essentially qualitative, ranking susceptibility without quantifying dynamic flow magnitudes. Consequently, they overlook the non-linear temporal dynamics of intense rainfall events and the specific connectivity of hillslope rills (Papaioannou et al.,
45 2018). To overcome these limitations, recent literature increasingly advocates rain-on-grid approach (e.g., Michailidi *et al.*, 2018; Ennouini *et al.*, 2024; Macchione *et al.*, 2026). Unlike static indices, these approaches simulate spatially resolved runoff responses, enabling the generation of hazard maps founded on quantitative values rather than qualitative proxies.

However, operationalizing these distributed models to address the specific challenge of Prediction in Ungauged Basins (PUB) requires tools that strike a balance between physical representativeness and parsimony (Hrachowitz et al., 2013). In this
50 context, the Hidropixel model has emerged as a promising tool (Costa et al., 2019; Veeck et al., 2020). In contrast to lumped models that average parameters over an entire basin, Hidropixel utilizes a fully distributed architecture where each grid cell functions as an independent micro-catchment. The model operates in a two-step process. First, it calculates the effective rainfall volume locally for every pixel using the Soil Conservation Service Curve Number (SCS-CN) method, based on soil type, land use, and antecedent moisture conditions (Mishra et al., 2004; Mishra and Singh, 2003; Sahu et al., 2012). Second, this local
55 volume is transformed into a specific runoff hydrograph using a pixel-dependent transfer function—typically a Triangular Unit Hydrograph (TUH). The timing of each pixel's hydrograph is governed by the travel time along the flow path from that specific cell to the catchment outlet, and the final basin response is obtained by aggregating all individual pixel hydrographs at the outlet. Most recently, Lima *et al.* (2024) upgraded the framework to the TUH+ version (Triangular Unit Hydrograph with lag parameter). This formulation refines the standard convolution process by integrating a time-lag parameter (T_v), which
60 explicitly accounts for the translation and storage effects inherent in runoff routing. By spatially varying the unit hydrograph parameters for every pixel, the TUH+ approach significantly enhances the simulation of hydrograph shape—specifically peak magnitude and timing (Lima et al., 2024).

Despite the model's structural strengths, its internal components require optimization for ungauged applications. Regarding runoff generation, the SCS-CN method remains the standard due to its computational simplicity, stability, and reliance on



65 accessible catchment data. While widely adopted (e.g. Neitsch *et al.*, 2011; Scharffenberg and Fleming, 2013), its conventional
application is still challenged by recent studies (Panigrahi and Ramadas, 2025; Soulis, 2021). One of the main criticisms
concerns the initial abstraction ratio (λ), traditionally fixed at 0.2. This value is often excessive for agricultural catchments,
leading to a systematic underestimation of runoff volumes for small-to-moderate rainfall events. Consequently, modern
adaptations—such as those proposed by Woodward *et al.* (2003), Jain *et al.* (2006), and Verma *et al.* (2017)—advocate for a
70 reduced $\lambda = 0.05$ or a calibrated relationship between initial abstraction (I_a) and potential retention (S). Moreover, the method's
inherent inability to explicitly account for rainfall intensity dynamics limits its physical realism during short, high-intensity
storms (Grimaldi *et al.*, 2013; Ponce and Hawkins, 1996). Therefore, implementing Hidropixel effectively requires moving
beyond standard parameters to systematically test these alternative CN formulations.

Equally critical to the flood response is the routing of this effective runoff, a process governed by the estimation of flow
75 velocity. Traditionally, this translation is parameterized via the concentration time (T_c), a metric fraught with epistemic
uncertainty (Grimaldi *et al.*, 2012; Michailidi *et al.*, 2018). Empirical formulas can yield results differing by nearly one order
of magnitude for the same catchment, drastically altering the resulting peak discharge (Q_p) and timing (T_p). To address the
limitations of lumped T_c equations, there is a specific need to integrate spatially explicit routing methods that derive velocity
directly from local topography and roughness, such as the SCS velocity method (USDA-NRCS, 2010) or the SWRRB
80 formulation (Williams *et al.*, 1985). The adoption of these methods is justified by their suitability for data-scarce environments
and their compatibility with high-resolution GIS datasets. Unlike lumped empirical equations—such as the Kirpich formula—
these formulations enable the characterization of a spatially explicit velocity field, capturing landscape heterogeneity through
pixel-specific slope and roughness parameters. Furthermore, in distributed models, the interplay between grid size and
hydraulic routing is pivotal. The spatial representation of the drainage network is scale dependent. Indeed, operating at high
85 spatial resolution is essential when applying these methods; coarser grid resolutions tend to smooth out slope gradients and
shorten flow paths, artificially accelerating or delaying concentration times, which compromises the routing accuracy
(Grimaldi *et al.*, 2012; Veeck *et al.*, 2020). However, these kinematic approximations are not without limitations. First, they
remain sensitive to roughness parameterization (Manning's n), which is difficult to validate in ungauged channels (Arcement
and Schneider, 1989). Second, and arguably more critical, is the issue of non-linearity. Standard velocity methods typically
90 impose a stationary travel time field determined exclusively by topography and roughness. This approach disregards the
hydrodynamic dependence of velocity on flow depth (Gericke and Smithers, 2014; Grimaldi *et al.*, 2012; Walega *et al.*,
2020), which can lead to substantial inaccuracies in hydrograph representation and an underestimation of peak flow timing
during extreme events (Michailidi *et al.*, 2018).

In light of this context, the primary goal of this study is to develop a robust methodology for high-resolution mapping of runoff
95 flood hazard by quantifying peak discharge distributions across ungauged catchments. To evaluate this framework, the
methodology is applied to an experimental agricultural catchment, providing a high-quality dataset to validate the model's
performance against observed rainfall-runoff events. Specifically, the research objectives are threefold:



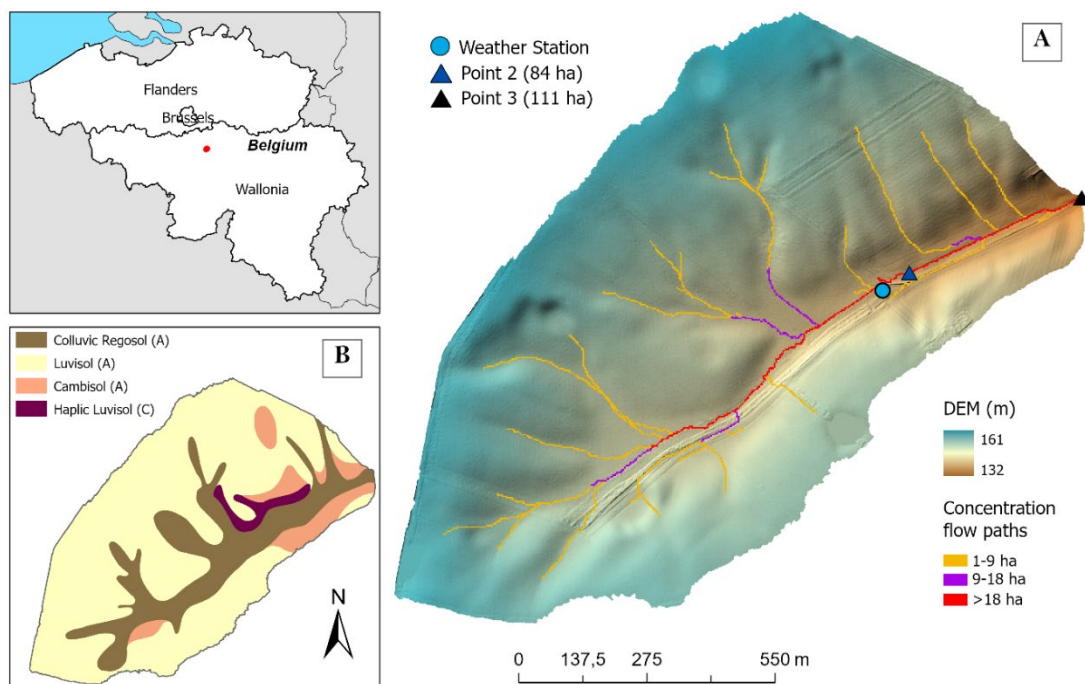
- i. Identify the most effective runoff calculation method by comparing several SCS-CN formulations (Standard, Jain, Woodward, and Hawkins) under both lumped and fully distributed modelling approaches.
- 100 ii. Determine the most accurate approach for calculating travel times by contrasting the SCS Velocity and SWRRB methods, leveraging high-resolution (1 m) topographic and land-use data.
- iii. Spatialize runoff flood hazard by utilizing the optimised model to generate fine-scale spatially distributed maps of peak flows along concentration paths for specific return periods.

2 Methodology

105 2.1 Study area

The study area is a headwater catchment located in Chastre, representative of the loess belt region of central Belgium (50°36'23,02"N, 4°35'42,33"E, Fig. 1). The Belgian loess belt is historically characterised by high rates of water-induced soil erosion and frequent pluvial, often muddy, flood events. The watershed has been extensively described and monitored in previous studies, notably by Pineux *et al.* (2017) and Cantreul *et al.* (2020), providing a robust dataset for validation, including
110 continuous hydrological observations since 2012. The catchment exhibits a gently undulating topography typical of the region, with elevations ranging from 132 to 161 m and gentle to moderate slopes varying between 0.25 and 17%, with a mean slope of 3.8%. The total catchment area (outlet = Point 3 in Fig. 1) covers 111 ha and contains a nested sub-catchment (Outlet = Point 2) of 84 ha. Morphologically, the basin is elongated, the longest hydraulic path (LHP) extending over 2,036 m from the main outlet (Point 3). Hydrologically, it functions as a "dry" valley, lacking a permanent river network and governed entirely
115 by episodic runoff dynamics.

The catchment is characterized by a temperate oceanic climate (Köppen–Geiger Cfb), with a long-term mean annual temperature of 10.3 °C and precipitation of 820 mm over the 1991–2020 reference period (IRM, 2023). Geologically, the catchment is underlain by thick Quaternary loess deposits that support Cambisols and Luvisols. These soils feature a clay-enriched B horizon which, although conducive to natural drainage, has been progressively truncated by diffuse erosion on the
120 hillslopes. Anthropogenic pressure is significant, with 98% of the area dedicated to arable land and negligible forest cover (0.11%). The landscape is emblematic of intensive open-field cropping systems, dominated by large parcels (on average 14.5 ha) where semi-natural features such as hedgerows are sparse. This specific configuration—intensive cultivation combined with the high susceptibility of loess soils to structural degradation (crusting)—renders the catchment highly prone to surface sealing and the rapid concentration of runoff along flow concentrated paths.



125

Figure 1. (A) Location of the study catchment and its two nested discharge monitoring points in Belgium. (B) Soil map classified according to the WRB reference groups. Superimposed letters denote the SCS Hydrologic Soil Groups used to parameterize runoff potential.

130

The nested configuration of the catchment facilitates a multi-site validation strategy. This setup allows peak discharge estimates to be verified at two distinct scales within the drainage network, thereby assessing the model's spatial consistency.

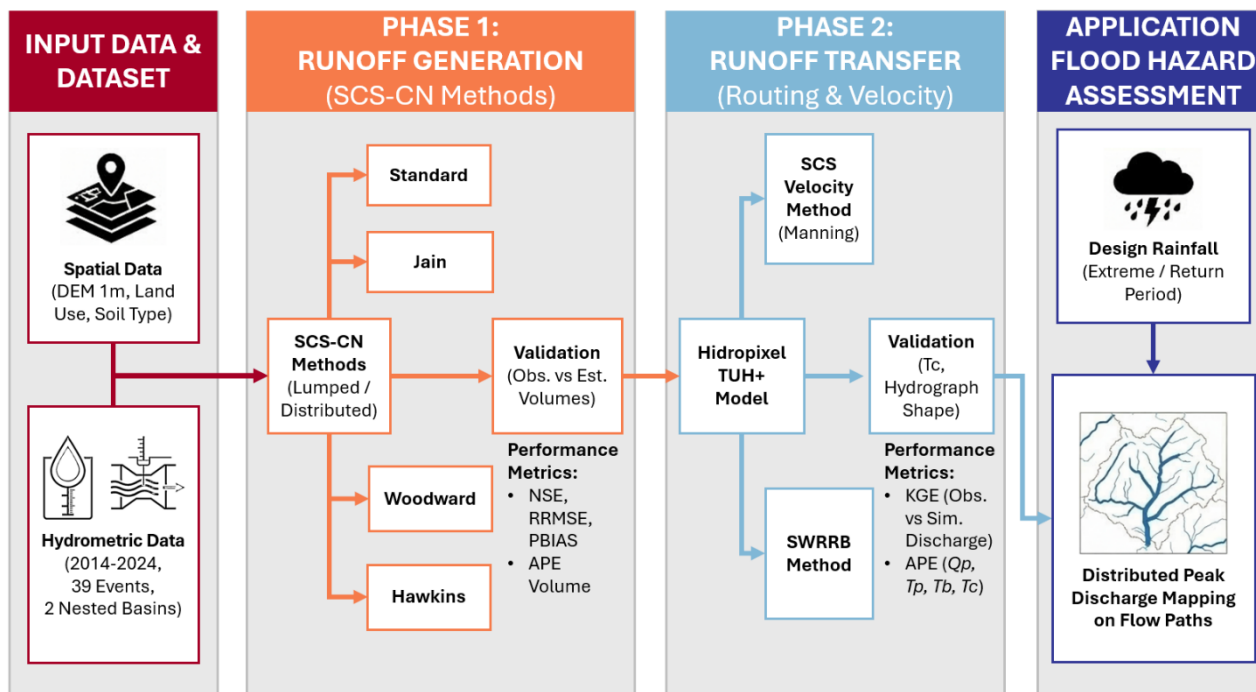
2.2 Methodological approach

135

To explore the potential of a robust framework for ungauged catchments, this study moves beyond site-specific calibration to focus on the spatial distribution of peak discharges along concentrated flow paths. The proposed methodological workflow (Fig. 2) utilizes the Hidropixel model (Lima *et al.*, 2024) at a 1 m resolution, structured around a systematic evaluation of (i) runoff generation and (ii) hydraulic transfer. This framework is tested against a dataset of 39 rainfall-runoff events from an experimental agricultural catchment. The validation follows a stepwise process: first assessing runoff volume accuracy under various initial abstraction hypotheses, then evaluating routing performance regarding peak timing and magnitude, before finally synthesizing these components into an operational tool for flood hazard mapping.

140

The runoff generation mechanism (Phase 1)—the conversion of raw rainfall into effective runoff volume—is evaluated by comparing alternative formulations of the Soil Conservation Service Curve Number (SCS-CN) method. To identify the most consistent approach for ungauged conditions in the study area, four distinct CN configurations (Sect. 2.2.1) are implemented, testing both lumped and distributed grid approaches. These configurations are assessed based on their ability to accurately reproduce observed runoff volumes across a diverse range of events (Sect. 2.4.5).



145 **Figure 2. Schematic overview of the methodological framework implemented in this study.**

The runoff transfer (Phase 2) is analysed by propagating the runoff produced by the optimal runoff generation SCS-CN method. This phase focuses on the temporal dynamics of the flow. Two distinct hydraulic strategies for estimating flow velocity and travel time are contrasted: the SCS velocity method and the SWRRB method. The validity of these routing schemes is determined by their capacity to predict the time of concentration (T_c), time to peak (T_p), and ultimately the peak discharge (Q_p) at the outlet.

150

Finally, the framework integrates these validated components to operationalise runoff flood hazard assessment. Using the optimal combination of production and transfer functions, the method generates a distributed map of peak discharges along concentration flow paths. To achieve this, the Hidropixel model is computationally optimised to be applied iteratively to every pixel along the defined concentration flow paths, treating each as an independent outlet. This allows for a precise, localised quantification of flood hazard at a high spatial resolution.

155

2.3 The Hidropixel modelling framework

Fundamentally, Hidropixel (Lima *et al.*, 2024) discretises the catchment into a regular grid, treating each pixel as an independent micro-basin. The operational structure of the model follows four sequential steps (Fig. 3): (1) the estimation of excess runoff per pixel, (2) the calculation of hydraulic travel time, (3) the routing of runoff using the TUH+ approach, and (4) the superposition of individual pixel hydrographs at the outlet. The specific mathematical formulations compared in this study for the generation (step 1) and transfer (step 2 & 3) phases are detailed in the following subsections.

160

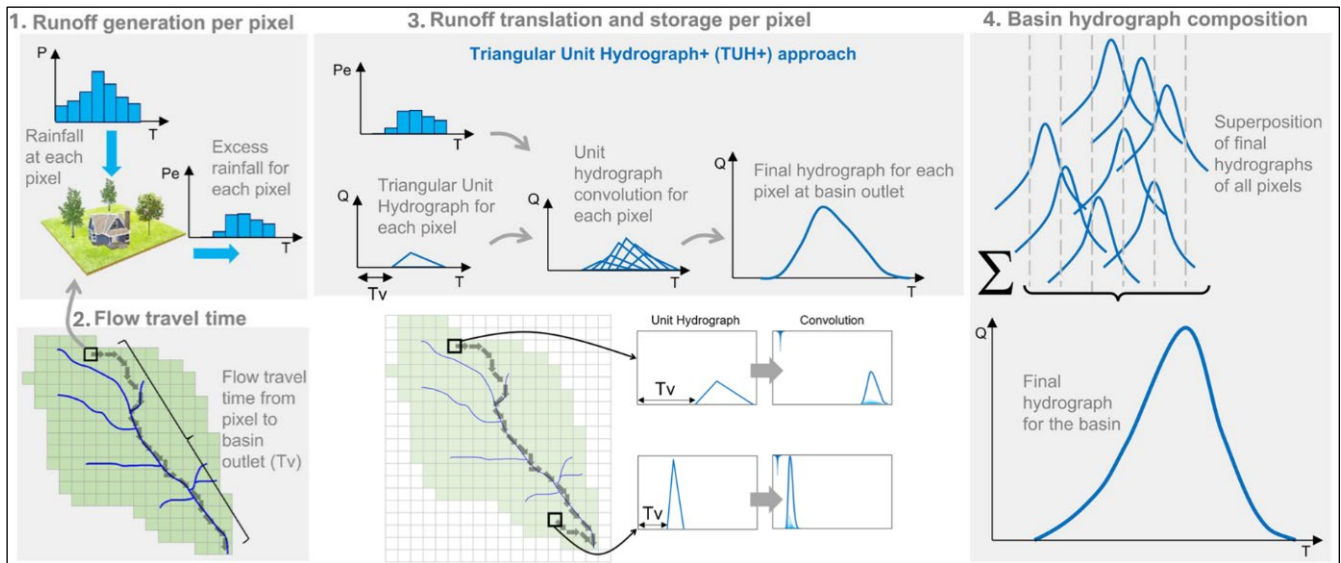


Figure 3. Schematic illustration of the Hidropixel model (based on Lima et al., 2024).

2.3.1 Runoff generation per pixel: SCS-CN method and derivatives

165 The model's initial module calculates effective rainfall volume at the pixel scale using the Soil Conservation Service Curve
 Number (SCS-CN) method. The CN is calculated on the available data: land use, soil hydrologic group, and antecedent
 moisture conditions (AMC). Regarding AMC, a normal state (CNII) is assumed for all simulations (Hawkins et al., 2008;
 USDA-NRCS, 2010).

The SCS-CN equations estimate surface runoff (Q) as a function of total precipitation (P) and the potential maximum retention
 170 (S), as defined by Eq. (1-3):

$$Q = \begin{cases} \frac{(P-I_a)^2}{P-I_a+S} & \text{when } P > I_a \\ 0 & \text{when } P \leq I_a \end{cases} \quad (1)$$

$$I_a = \lambda S \quad (2)$$

$$S = \frac{25400}{CN} - 254 \quad (3)$$

Where P , Q , I_a (initial abstraction), and S are expressed in mm. In the standard method, I_a is conceptually linked to storage
 175 by a fixed ratio, λ .

Modifying λ requires adjusting S , as standard CN tables were originally calibrated for $\lambda = 0.2$. To identify the most accurate
 approach for ungauged conditions, this study evaluates four distinct SCS-CN formulations:

- 1) **Standard Method** ($\lambda = 0.2$): The classical approach using the original unadjusted S derived from standard CN tables.



- 2) **Hawkins Method** ($\lambda = 0.05$): This approach adopts a reduced initial abstraction ratio and adjusts the relationship
180 between $S_{0.05}$ and the standard $S_{0.2}$ using the linear conversion proposed by Hawkins *et al.* (2008):

$$S_{0.05} = 1.42 S_{0.2} \quad (4)$$

- 3) **Woodward Method** ($\lambda = 0.05$): This method employs a non-linear conversion derived by Woodward *et al.* (2003)
from a massive dataset of 28,301 events across 307 US catchments:

$$S_{0.05} = 0.8187 (S_{0.2})^{1.15} \quad (5)$$

- 4) **Jain Method**: Unlike the previous methods which assume a constant I_a , Jain *et al.* (2006) proposed a generalized
185 relation where I_a depends on rainfall intensity. Calibrated on 22,392 events, this formulation showed superior
performance with parameter values of $\lambda = 0.3$ and $\alpha = 1.5$:

$$I_a = \lambda S \left(\frac{P}{P+S} \right)^\alpha \quad (6)$$

Each of the four SCS-CN derivations is evaluated under two configurations: a classic lumped application, where CN is area-
190 weighted average at the basin scale yielding a uniform runoff depth, and a distributed application within Hidropixel.

2.3.2 Flow travel time

Once the runoff volume is generated, the model determines the time required for a water particle to travel from each pixel to
the catchment outlet (T_v). Addressing the specific recommendation by Veeck *et al.* (2020) to explore alternative routing
formulations in Hidropixel, this study evaluates two distinct approaches for estimating travel time. We test two indirect
195 hydraulic formulations—(a) the distributed SCS velocity method, which is the standard Hidropixel approach and (b) the
SWRRB method. Additionally, we integrate (c) an intensity-dependent adjustment of T_v for extreme events ($T > 2$ years),
accounting for faster flow velocities during heavy rainfall.

(a) SCS velocity method

The SCS velocity method segments the flow path into three distinct regimes based on hydraulic thresholds: sheet flow, shallow
200 concentrated flow, and open channel flow (USDA-NRCS, 2010). Sheet flow is assumed to occur over the first 30 m of the
hillslope, where travel time (T_s) is calculated by Eq. (7) using a kinematic wave approximation sensitive to surface roughness.
Beyond this distance, flow transitions to shallow concentrated flow (e.g., rills and gullies), where velocity is a function of the
square root of the slope (Eq. 8). To prevent unrealistic flow velocities in steep terrain, velocities are explicitly bounded between
0.02 and 2.0 m s⁻¹ following Grimaldi *et al.* (2010). Finally, open channel flow is modelled using Manning's equation within
205 the permanent drainage network (Eq. 9). The total travel time for any given pixel i is calculated by summing the transit times
of all successive cells along the hydraulic flow path to the outlet (Eq. 10).



$$T_{s_i} = \frac{5.474 (L_i n_i)^{0.8}}{P_{24}^{0.5} I_i^{0.5}} \quad (7)$$

$$T_{sc_i} = \frac{L_i}{V_i}, \text{ where } V_i = k_i I_i^{0.5} \quad (8)$$

$$T_{cc_i} = \frac{L_i}{V_i}, \text{ where } V_i = \frac{Rh_i^{2/3} I_i^{1/2}}{n_i} \quad (9)$$

$$210 \quad T_{v_i} = \sum_{i=1}^{N_s} T_{s_i} + \sum_{i=1}^{N_{sc}} T_{sc_i} + \sum_{i=1}^{N_{cc}} T_{cc_i} \quad (10)$$

Where T_{v_i} is the total travel time of the i -th pixel (min), representing the sum of travel times across the operative flow regimes: sheet flow (T_{s_i}), shallow concentrated flow (T_{sc_i}), and open channel flow (T_{cc_i}). L_i is the flow length across the pixel (m), corresponding to the pixel side length for orthogonal flow, or $\sqrt{2}$ times the side length for diagonal flow directions; V_i is the pixel velocity (m s^{-1}); I_i is the pixel slope (m m^{-1}); P_{24} is the rainfall depth for the 24-h duration and 2-year return period (mm); n_i is the pixel-specific Manning's roughness coefficient; k_i is a local routing coefficient derived from the simplification of Eq. (9), assuming a constant hydraulic radius and roughness for specific land covers under a wide-channel hypothesis (USDA-NRCS, 2010); Rh_i is the hydraulic radius (m) of the i -th pixel, defined as the ratio of the cross-sectional area of flow to its wetted perimeter; and N represents the number of downstream pixels in each respective flow regime.

215 In the standard NRCS formulation, shallow concentrated flow velocity is estimated assuming a constant flow depth of approximately 7.6 cm (0.25 ft), or up to 12.2 cm (0.4 ft) for grassed waterways. While this assumption is suitable for coarse-resolution DEMs (e.g., 30 m) where micro-topography is smoothed, it becomes inconsistent in high-resolution modelling of dry valleys. Indeed, reducing DEM resolution inevitably extends flow path lengths (Grimaldi et al., 2012; Moglen and Hartman, 2001). Without a corresponding adjustment in hydraulic parameters, this mechanical increase in path length leads to a systematic overestimation of travel times. Furthermore, in the specific context of Walloon dry valleys, the shallow flow regime often extends over significant distances. Treating these zones with a fixed, shallow depth fails to account for the progressive concentration of flow and the associated increase in hydraulic radius.

225 Field observations from the Chastre experimental catchment confirmed that flow depths progressively increase as runoff concentrates, reaching 14 cm at a 4-ha sub-catchment outlet and exceeding 70 cm within the main terminal channel of the 111 ha basin. To accurately represent this geomorphological continuum from hillslope runoff to channelized flow, the constant 7.6 cm shallow depth assumption was empirically adjusted. A site-specific, stepwise area-to-depth relationship was calibrated based on the contributing area (Ac):

- $Ac < 5$ ha: 7.6 cm (Standard shallow concentrated flow)
- $5 < Ac < 50$ ha: 12.2 cm (Deepening concentrated flow)
- $50 < Ac < 100$ ha: 20.0 cm (Transition to open channel flow)
- 235 • $Ac > 100$ ha: 30.0 cm (Established open channel flow)



This local reclassification successfully identifies the dynamic transition from shallow to channel flow. It overcomes the limitations of the fixed shallow routing coefficient (k) in high-accumulation thalwegs, ensuring a more realistic routing process consistent with local observations.

(b) SWRRB method

240 As an alternative to the distributed NRCS approach, the SWRRB method (Williams et al., 1985) offers a semi-empirical formulation commonly utilised in basin-scale models. SWRRB estimates the total time for each pixel as the aggregate of a hillslope component (T_{s_i}), dependent on sheet flow characteristics, and a channel component (T_{cc_i}), which is a function of the basin's morphometry. This method is tested here to evaluate whether a simplified routing scheme can perform adequately within a high-resolution modelling framework. The hillslope travel time (Eq. 11) and channel travel time (Eq. 12) are calculated
245 as follows:

$$T_{s_i} = \frac{(L_i n_i)^{0.6}}{18 I_i^{0.3}} \quad (11)$$

$$T_{cc_i} = \frac{0.62 L_{c_i} n_i^{0.75}}{A_i^{0.125} I_i^{0.375}} \quad (12)$$

$$T_{v_i} = T_{s_i} + T_{cc_i} \quad (13)$$

The method is applied using averaged parameters for each flow type. The variables are defined as follows: T_{s_i} and T_{cc_i}
250 represent the travel times (h) across the i -th pixel for sheet flow and open channel flow, respectively; L_i is the flow length (m); L_{c_i} is the channel length (km); n_i represents the Manning's roughness coefficient average along the flow path L ; I_i is the average slope of the flow path L (m m^{-1}), calculated as the total elevation difference divided by the flow length L ; A_i corresponds to the contributing area of pixel i (ha).

Consistent with the NRCS formulation described previously, a critical flow length threshold of 30 m is applied to distinguish
255 between sheet flow and channelized flow. This criterion is physically justified by the inherent instability of sheet flow, which tends to concentrate rapidly into rills due to micro-topographic irregularities. Pure surface sheet flow rarely exceeds 30 m before transitioning to a concentrated regime (McCuen and Spiess, 1995; USDA-NRCS, 2010).

Finally, to mitigate numerical artifacts associated with flat areas—which are more prevalent in high-resolution digital elevation models—a minimum slope of 0.005 m m^{-1} is imposed for travel time calculations (Fig. A1).

260 (c) Adjustment of T_v

A critical physical limitation in static routing models is the assumption of constant flow velocity regardless of storm magnitude. However, for extreme events, flow velocities increase significantly due to greater flow depths. As demonstrated by (Grimaldi et al., 2012; Michailidi et al., 2018), flow velocities increase—and consequently, T_c decreases—as the return period (T) and rainfall intensity increase. Using a fixed T_v derived from frequent events (e.g., 2-year rainfall) would therefore underestimate
265 peak flows for extreme storms (e.g., 100-year events).



To account for this non-linearity, this study adopts the kinematic wave scaling approach proposed by Meyersohn (2016). This method adjusts the reference travel time based on the ratio of effective rainfall intensities:

$$T_v = T_{v,R} \left(\frac{E}{E_R} \right)^m \quad (14)$$

Where T_v is the adjusted travel time for the specific return period T ; $T_{v,R}$ is the reference travel time calculated in the standard
270 Hidropixel run (based on 2-year rainfall parameters); E is the effective rainfall intensity of the extreme event; E_R is the effective rainfall intensity of the reference event; m is a dimensionless kinematic wave parameter dependent on flow geometry.

Following Meyersohn (2016), the exponent m is set to -0.4 for sheet flow and wide rectangular paths (representing overland
flow), and -0.3 for channel flow, assuming a trapezoidal channel geometry typical of the concentrated flow paths in the study
275 area. Preliminary sensitivity tests conducted on extreme rainfall events within this specific catchment confirmed that incorporating this adjustment yields superior T_v restitution compared to static methods (data not shown).

2.3.3 Triangular unit hydrograph (TUH)

The final stage of the modelling framework converts the excess rainfall volume and travel time calculated for each pixel into a specific discharge response at the catchment outlet.

In this distributed framework, a specific TUH is generated for every pixel i . Central to the TUH+ enhancements (Lima *et al.*,
280 2024), the travel time determined in the previous step drives the entire shape of the hydrograph. It influences not only the temporal delay (translation) but also the attenuation of the signal (storage). Pixels located further from the outlet—having larger T_v values—generate TUHs with longer time-to-peak and lower peak discharges. This mechanism allows the model to physically represent the increased storage and diffusion effects associated with longer flow paths.

$$T_{p_i} = \frac{d}{2} + 0.6 T_{v_i} \quad (15)$$

$$285 \quad T_{b_i} = 2.67 T_{p_i} \quad (16)$$

$$Q_{p_i} = 0.208 \left(\frac{A_i}{T_{p_i}} \right) \quad (17)$$

In these expressions, the subscript i denotes the specific pixel index. The temporal parameters T_{p_i} (time-to-peak) and T_{b_i} (base time), along with the excess rainfall duration d , are expressed in hours (h). The peak discharge Q_{p_i} is given in m^3/s , proportional to the contributing pixel area A_i (km^2).

290 2.3.4 Final hydrograph for the catchment

The final hydrograph at the outlet is generated by convolving the excess rainfall volume (step 1) with the generated Unit Hydrograph for each pixel (step 3). This step sums the individual contributions of every grid cell across the catchment. By



doing so, the flow is explicitly lagged by the travel time (step 2) and dispersed by the shape of the TUH transfer function, resulting in a spatially integrated runoff response.

$$295 \quad Q_{tot}(t) = \sum_{i=1}^{N_p} Q(t)_i \quad (18)$$

2.3.5 Computational optimization for high-resolution modelling

Applying the distributed TUH+ approach at a 1-m resolution entails a substantial computational load, as our 111-ha study catchment is discretized into over a million active cells. A cell-by-cell convolution would be computationally prohibitive. To address this, a grouped convolution strategy is implemented. The algorithm identifies unique combinations of CN and T_v across the catchment. Instead of computing the convolution integral for every individual pixel, pixels sharing identical hydraulic properties (CN) and routing delays (T_v) are aggregated into a single computational unit. The unit hydrograph is generated once for each unique (CN, T_v) pair and subsequently scaled by the total contributing area of the associated cluster. This approach reduces the number of required operations by several orders of magnitude, making the 1-m resolution modelling feasible without compromising the fully distributed nature of the results.

305 To maximize the efficiency of the grouping algorithm, the continuous variables are discretized: CN and T_v values are rounded up to the nearest integer, thereby reducing the number of unique computational pairs.

2.4 Calculation of flood risk from runoff: Spatialisation of peak flows

2.4.1 Rainfall

To drive the rainfall scenario simulations, the meteorological forcing is represented by a double-triangle design storm hyetograph, a standard methodological approach developed in France (Chocat et al., 1981). The temporal distribution of this synthetic storm relies on site-specific Montana coefficients, which are officially available at the municipal scale for the entire territory (<https://www.meteo.be/fr/climat/climat-de-la-belgique/climat-dans-votre-commune>), to specifically calculate and construct the dual-intensity peaks, providing a standardized critical rainfall profile for unmonitored areas.

2.4.2 Flood hazard map

315 Unlike traditional lumped approaches that provide hydrographs solely at the basin outlet, this framework extends the modelling scope to map flood hazard across the entire catchment. The model computes the peak discharge (Q_p) for every pixel located along the identified concentrated flow paths, which were delineated using a minimum flow accumulation threshold of 0.5 ha. In this procedure, the routing algorithm iterates through the drainage network, treating each pixel as a temporary outlet that aggregates the runoff from its specific upstream contributing area. This allows for the identification of critical discharge points often missed by standard outlet-focused simulations.

320 Technically, this is implemented by dynamically offsetting the global travel time map relative to the target location. For every target pixel considered as a temporary outlet, the global travel time map is adjusted by subtracting the total travel time value



(T_{v_i}) of that specific target pixel from the total travel time values of all upstream contributing pixels. This operation effectively resets the downstream boundary condition ($T_{v=0}$) to the location of the target pixel, simulating it as the new unique outlet for the convolution process.

2.5 Application of the model

2.5.1 Pre-processing of the digital elevation model (DEM)

The primary topographical input for this study is the high-resolution LiDAR Digital Elevation Model (DEM) covering the Walloon region of Belgium (2021-2022, available on <https://geoportail.wallonie.be>). Originally acquired at a 0.5 m resolution, the data was aggregated to 1 m. A critical aspect of distributed modelling is the sensitivity to DEM resolution. While the Hidropixel framework has demonstrated robustness at coarser scales (10–30 m), the increasing availability of high-resolution LiDAR data offers the opportunity to model flow paths with meter-scale precision. However, this increase in resolution presents a trade-off: as noted by Tarolli (2014), ultra-high resolutions can introduce excessive noise from micro-topographic artifacts without necessarily yielding proportional hydrological gains. In the specific context of Hidropixel, Veeck *et al.* (2020) analysed scale dependencies. They confirmed that, while coarser resolutions smooth out peak flows, finer grids are essential for capturing realistic travel times and flow connectivity. These observations align with findings by Thomas *et al.* (2017) and Cantreul *et al.* (2018), who identify the 1 m threshold as an optimum for delineating hydrologically sensitive zones while avoiding the over-sensitivity to micro-topographic variations. Furthermore, Alexopoulos *et al.* (2024) recently demonstrated a sharp degradation in hydraulic accuracy when coarsening grids from 1 m to 5 m. Consequently, this study adopts a 1 m resolution to best represent flow path variability while maintaining computational feasibility (Murphy *et al.*, 2008; Vaze *et al.*, 2010).

To simulate surface runoff, the raw DEM must be pre-processed to ensure hydrological continuity (i.e., removal of sinks and digital dams) (Jenson and Domingue, 1988; O'Callaghan and Mark, 1984). However, applying standard "sink filling" algorithms to high-resolution topography is known to introduce significant artifacts. As noted by Lidberg *et al.* (2017), pure filling tends to create artificial flat surfaces and linear flow paths that deviate from natural drainage patterns.

To mitigate these artifacts, a composite hydro-conditioning workflow was implemented using the WhiteboxTools geospatial library (Lindsay, 2016). Instead of relying solely on filling, this approach prioritizes breaching (lowering channel obstructions) to preserve the natural nuances of the landscape.

2.5.2 Land use and soil properties

To accurately characterize surface roughness and runoff potential, a composite land use map was generated by merging two complementary high-resolution datasets.

- The primary source for arable land is the Land Parcel Identification System (SIGEC). This vector dataset provides an annual inventory of declared agricultural parcels, distinguishing between specific crop types, productive arable land,



355 and non-productive features such as permanent grasslands, fallows, and grass buffer strips (https://geoportail.wallonie.be).

- For non-agricultural areas, the LifeWatch Wallonia land cover map (Radoux et al., 2022) is used at a 2-m spatial resolution to capture the remaining topographic features (forests, urban areas, water bodies).

360 Hydrological parameters (CN, Manning’s n) associated with general land cover classes are detailed in Table 1, derived from standard literature (Chow et al., 1988; Schneider & McCuen, 2005; SCS, 1972; USDA-NRCS, 2010). Given the high granularity of the SIGEC dataset, which contains more than 150 distinct crop classes, the full lookup table is not presented here. However, specific values for these crops were assigned using USDA-NRCS (2010), supplemented by CN values from the EPICgrid model (Sohier et al., 2009).

365 **Table 1. Summary of model parameters. The table presents Curve Number (CN) values cross-referenced by land use and Hydrologic Soil Group (A–D), alongside Manning’s roughness coefficients (n) categorized by flow type.**

Land Use	Categories	CN (A) ^{1 2}	CN (B)	CN (C)	CN (D)	Manning (n)		
						Sheet flow ^{2 3}	Shallow concentrated flow ³	Channel flow ⁴
Map Class LifeWatch								
Building, specific structures and facilities	Building	99	99	99	99	0.015	0.015	0.01
Artificially sealed ground surface	Artificial surface	99	99	99	99	0.015	0.015	0.01
Natural Material Surfaces with less than 10% vegetation	Bare soil	77	86	91	94	0.034	0.034	0.02
Water	Water	99	99	99	99	0.018	0.018	0.02
Forest	Forest	36	60	73	79	0.269	0.136	0.10
Vegetation of recently disturbed area (e.g., clear cut)	Temporary grassland	49	69	79	84	0.101	0.049	0.04
Sparse vegetation	Temporary grassland	49	69	79	84	0.101	0.049	0.04
Inundated grassland and scrub of biological interest	Permanent grassland	49	69	79	84	0.162	0.068	0.04
Grassland and scrub of biological interest	Permanent grassland	49	69	79	84	0.162	0.068	0.04
Herbaceous vegetation in rotation during the year (e.g., crops)	Crops	65	76	84	88	0.088	0.039	0.03
SIGEC*								
Winter wheat	Crops	63	75	83	87	0.088	0.039	0.04
Sugar beet	Crops	67	78	85	89	0.088	0.039	0.03

¹Sohier and Degre, 2011; ²USDA-NRCS, 2010; ³McCuen *et al.*, 1996; ⁴Chow, 1959.

* Non-exhaustive list.

The Hydrologic Soil Groups required for the CN method are derived from the Walloon soil infiltrability map (Demarcin et al., 2011). This dataset classifies soils into four standard groups (A, B, C, and D) based on their minimum infiltration rate, which



is determined by pedological characteristics including soil texture, depth to bedrock, stratification, and natural drainage
370 capacity.

2.5.3 Hydrometeorological data and event selection

To calibrate and validate the models, a monitoring dataset was compiled from the experimental watershed at Chastre
(encompassing sub-catchments Point 2 and Point 3; see Sect. 2.1). The precipitation data was recorded using a high-precision
weighing rain gauge (OTT Pluvio² L) located near the outlet of the 111 ha sub-catchment (Point 2). This device provides data
375 at a 5-minute temporal resolution, ensuring accurate capture of peak intensities.

Coincident streamflow series were derived from a continuous monitoring network adapted to local channel morphologies.
Runoff at controlled outlets was monitored using gauging flumes (e.g., San Dimas type), where water levels were converted
to discharge using site-specific stage-discharge relationships. For simple channel sections without structural controls, discharge
was continuously computed by coupling water level measurements with acoustic Doppler velocity sensors. All discharge
380 datasets were recorded and synchronized with rainfall data at a 5-minute time step to ensure precise lag-time analysis.

The study utilizes a total of 39 rainfall-runoff events recorded between 2014 and 2024 (Table B1). To ensure hydrological
relevance, events were included only if they met this rainfall depth and generated measurable discharge at either gauging
station. In addition, the analysis was restricted to short-duration rainfalls (<24 h) to align with the fundamental assumption of
the standard SCS-CN method, which is designed for single-event simulations and inherently neglects continuous inter-storm
385 drainage and evapotranspiration processes (Mishra and Singh, 2003; Ponce and Hawkins, 1996).

The return period (T) of each storm was determined based on the total amount and duration of the rainfall events using the
official Intensity-Duration-Frequency (IDF) curves for the catchment location (Royal Meteorological Institute of Belgium,
RMI). Out of the 39 events, 35 events are hereafter considered as normal events ($T < 2$ years) whereas 4 events with $T \geq 2$
years will be referred to as extreme events.

390 To confront the indirect routing configurations (SCS and SWRRB, see Sect. 2.3.2), a reference time of concentration (T_c),
defined as the travel time from the hydraulically most distant pixel to the catchment outlet, is derived directly from the observed
rainfall-runoff events. This study employs the inflection point method to define T_c as the time interval between the cessation
of effective rainfall and the inflection point on the hydrograph's recession limb (Gericke and and Smithers, 2014; McCuen,
2009).

395 Identifying this point is critical in the specific context of the studied dry valleys. Since the hydrological regime is ephemeral
($Q_{base} \approx 0$), baseflow separation is not required. However, determining the exact cessation of direct runoff remains challenging
due to the asymptotic nature of the recession curve, which reflects slow channel depletion. To resolve this, the inflection point
is identified by analysing the second derivative of the smoothed discharge time series ($d^2Q/dt^2 = 0$). This provides a physically-
based indicator that marks the transition from active surface runoff contributions to the passive draining of channel storage
400 (Nejadhashemi et al., 2007).



2.5.4 Model performance evaluation criteria

As recommended by numerous researchers (e.g., Fentie *et al.*, 2002; Moriasi *et al.*, 2015), a multi-criteria approach was adopted to ensure a comprehensive evaluation of the hydrological model performance. The Kling-Gupta Efficiency (KGE; Kling *et al.*, 2012) serves as the primary goodness-of-fit statistic, providing a balanced assessment of correlation, variability, and bias. This is complemented by the Nash-Sutcliffe Efficiency (NSE) to evaluate overall hydrograph agreement, the Relative Root Mean Square Error (RRMSE) to quantify the residual variance, and the Percent Bias (PBIAS) to identify any systematic over- or underestimation tendencies.

Furthermore, to evaluate the overall accuracy of the hydrograph reproduction, four event-based metrics are computed. While the relative volume error (δV) assesses the total runoff generation, the quality of the routing process is specifically measured by the relative time-to-peak error (δTp) and base time error (δTb), which reflect temporal synchronization and flow attenuation. The relative peak discharge error (δQp) evaluates the resulting flood magnitude. All four metrics are expressed as the normalized difference between simulated and observed values.

3. Results & Discussion

3.1 Runoff generation

The evaluation of runoff volume generation, summarized in Table 2 and illustrated by the error distributions in Fig. 4, reveals significant disparities depending on the chosen volumetric method and, to a lesser extent, the spatial modelling approach. The analysis of efficiency criteria highlights the inadequacy of the Standard (SCS-CN) method for this catchment. With an average negative NSE of -0.32 and a bias of -91%, this method leads to a severe systematic underestimation of flow volumes. Figure 4 corroborates this by showing an error distribution collapsed towards -100%, with a high density of crosses. These markers indicate that the precipitation depth did not exceed the initial abstraction ($P < Ia$), resulting in zero simulated runoff despite observed flow. This aligns with findings by Woodward *et al.* (2003) and Baltas *et al.* (2007), who demonstrated that the standard ratio ($\lambda = 0.2$) tends to overestimate Ia in agricultural catchments, thereby preventing runoff initiation for low magnitude rainfall events.

Table 2. Performance metrics for runoff volume estimation across 39 events. Comparison of four volumetric methods (Standard, Hawkins, Woodward, Jain) applied to both distributed (Hidropixel) and lumped modelling frameworks.

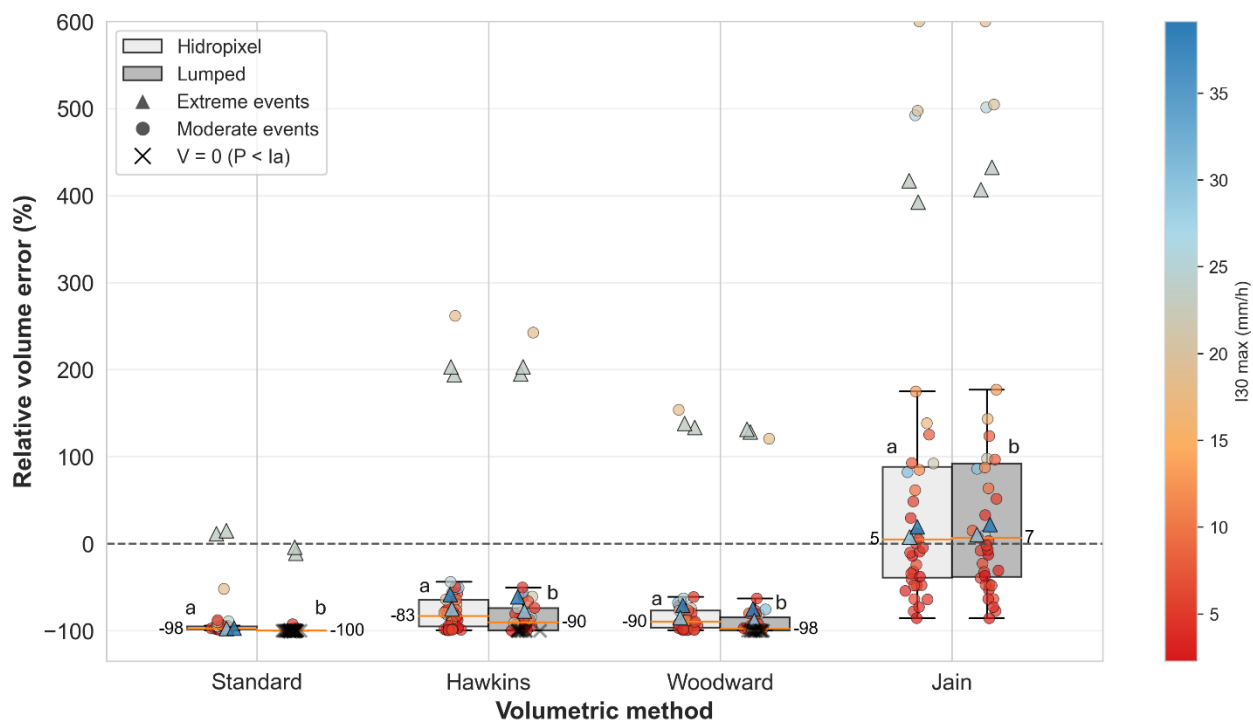
	Standard		Hawkins		Woodward		Jain	
	Lumped	Hidropixel	Lumped	Hidropixel	Lumped	Hidropixel	Lumped	Hidropixel
NSE	-0.36	-0.28	0.08	0.10	-0.02	0.02	0.14	0.17
RRMSE (%)	170	165	140	138	147	144	135	133
PBIAS (%)	-93	-89	-61	-59	-73	-70	19	16



Methods incorporating an adjusted initial abstraction ratio—Woodward and Hawkins—improve upon the standard approach but still struggle with substantial volume deficits. While Woodward reduces the negative bias to approximately -71%, Hawkins further mitigates the underestimation (bias near -60%) and manages to produce slightly positive NSE values (up to 0.10).
 430 Although these approaches confirm the necessity of calibrating the $I_a - S$ relationship rather than relying on default handbook values (Baltas *et al.*, 2007; Baert *et al.*, 2026: currently being published), they remain insufficient for accurate volume restitution in this specific basin.

Conversely, the Jain method emerges as the most robust and suitable approach for volume estimation. It achieves the highest overall performance, yielding the best NSE (0.17) and the lowest relative error (RRMSE of 133%). Unlike the other methods
 435 that systematically underestimate runoff, the Jain method provides a much more balanced volume generation, displaying only a slight positive bias (16.4%).

Furthermore, across all tested volumetric methods, the distributed Hidropixel model consistently outperforms the lumped approach, delivering a statistically significant improvement in runoff generation ($p < 0.05$, Wilcoxon signed-rank test). Quantitatively, the distributed framework yields higher NSE, lower RRMSE, and reduced bias, alongside error medians closer
 440 to zero and narrower interquartile ranges (Table 2; Fig. 4). This consistent superiority highlights the added value of spatially resolving the runoff process: explicitly accounting for the spatial heterogeneity of the CN allows for a more realistic identification of active contributing areas, whereas the lumped approach artificially dampens these localized responses through basin-wide averaging.





445 **Figure 4. Comparative boxplots of signed relative volume error (%) for runoff events (n = 39) at the Chastre watershed using the**
Hidropixel model (light grey) and a lumped model approach (grey). Marker shapes distinguish event categories (circles for normal
events, triangles for extreme events), while the colour gradient indicates the I30 max (the maximum intensity of rainfall recorded
over a period of 30 minutes), and the black crosses highlight zero-runoff simulations (P < Ia). Numeric median values are displayed.
Different lowercase letters (a, b) indicate statistically significant differences between the distributed and lumped models (Wilcoxon
 450 **signed-rank test).**

A deeper analysis using Spearman rank correlation dissects the drivers behind these performance disparities between methods (Table 3). For the Standard, Hawkins, and Woodward methods, the volumetric error exhibits a very strong, highly significant positive correlation with total rainfall depth ($\rho = 0.67$ to 0.85). This indicates a structural bias where the error scales directly with storm size. The Jain method significantly mitigates this issue, outperforming the others by effectively halving this
 455 dependency on total rainfall ($\rho = 0.47$). This superiority stems from Jain’s specific formulation, which explicitly incorporates the precipitation depth into the determination of the initial abstraction or potential maximum retention (Eq. 6). By making the abstraction dynamically dependent on the storm size rather than relying on a static linear ratio, the Jain method adapts much better to varying rainfall magnitudes. Interestingly, rainfall duration showed no significant correlation with volumetric error, further isolating intensity and volume as the primary meteorological drivers.

460 **Table 3. Spearman rank correlation coefficients (ρ) between the relative volumetric error of the four SCS-CN configurations and key hydro-meteorological drivers. I30 max refers to the maximum intensity of rainfall recorded over a period of 30 minutes and P5 is the 5-day antecedent rainfall.**

	Relative volumetric error			
	Standard	Hawkins	Woodward	Jain
Rainfall (mm)	0.67 **	0.85 **	0.83 **	0.47 **
I30 max (mm/h)	0.64 **	0.63 **	0.65 **	0.71 **
P5 (mm)	-0.19	-0.17	-0.15	-0.12
Duration of rainfall (min)	-0.09	0.01	-0.03	-0.28

*p < 0.05; ** p < 0.01

Spearman analysis reveals a persistent structural limitation across all methods: the error remains strongly correlated with the maximum 30-minute rainfall intensity (*I30max*), peaking with Jain ($\rho = 0.71$). This dependency exposes a well-known flaw in
 465 the classical SCS-CN framework, which relies solely on cumulative rainfall volume and ignores temporal intensity (Grimaldi et al., 2013; Ponce and Hawkins, 1996). Consequently, the model cannot distinguish between prolonged low-intensity rain and violent storms, structurally failing to capture Hortonian (infiltration-excess) runoff.

Beyond rainfall characteristics, the mixed performance is heavily driven by the model's structural inability to dynamically account for initial catchment conditions. In this study, all simulations were parameterized using a normal moisture state (CNII),
 470 deliberately excluding the traditional 5-day antecedent rainfall (P5) adjustment. Our Spearman analysis statistically supports this decision, as P5 exhibited no significant correlation with the relative volume error. This findings aligns with updated guidelines, which explicitly discourage the use of P5 due to a proven lack of statistical correlation with observed CN variations (Hawkins et al., 2008; USDA-NRCS, 2010). Consequently, the model operates entirely independently of the real pre-storm saturation level. As highlighted by Michel *et al.* (2005) and Brocca *et al.* (2012), without a continuous Soil Moisture



475 Accounting (SMA) module to track the actual saturation deficit, the CN framework remains overly rigid. It introduces severe
systematic biases whenever the assumed static CNII state misaligns with the true initial moisture conditions of the catchment.
This lack of temporal flexibility extends beyond short-term moisture to the seasonal scale. By utilizing a fixed annual CN, the
model treats the catchment surface identically in winter (bare soil) and summer (fully developed canopy), entirely neglecting
the evolution of crop cover and soil crusting. However, observed CNs exhibit distinct seasonal patterns, typically decreasing
480 during the growing season as canopy interception and evapotranspiration increase (Hjelmfelt, 1991). While specific
formulations exist to dynamically adjust the CN based on vegetation cover and crusting stages (e.g., Van Oost, 2003), they
require highly localized and temporally continuous field data that are rarely available. Furthermore, as demonstrated in the
appendix (Fig. C1), applying these data-intensive dynamic adjustments to our dataset did not yield superior performance
compared to the Jain method.

485 In summary, the model's mixed performance is physically deterministic: the static CN equation inherently struggles to
reproduce runoff whenever the generation mechanism is dominated by highly dynamic factors—specifically rainfall intensity,
storm duration, variable antecedent moisture, and crop cover—that the conceptual framework does not explicitly resolve.
While these structural limitations could invite a fundamental recalibration of the method (e.g., through context-specific
adjustments of λ , as showed in Appendix C), such a pursuit would conflict with the objective of maintaining a parsimonious
490 tool for ungauged basins, where the data required for more complex formulations are non-existent. Nonetheless, the ability of
this framework to produce acceptable runoff predictions without requiring any empirical parameter calibration underscores its
critical operational value for poorly gauged or ungauged agricultural basins.

3.2 Runoff transfer

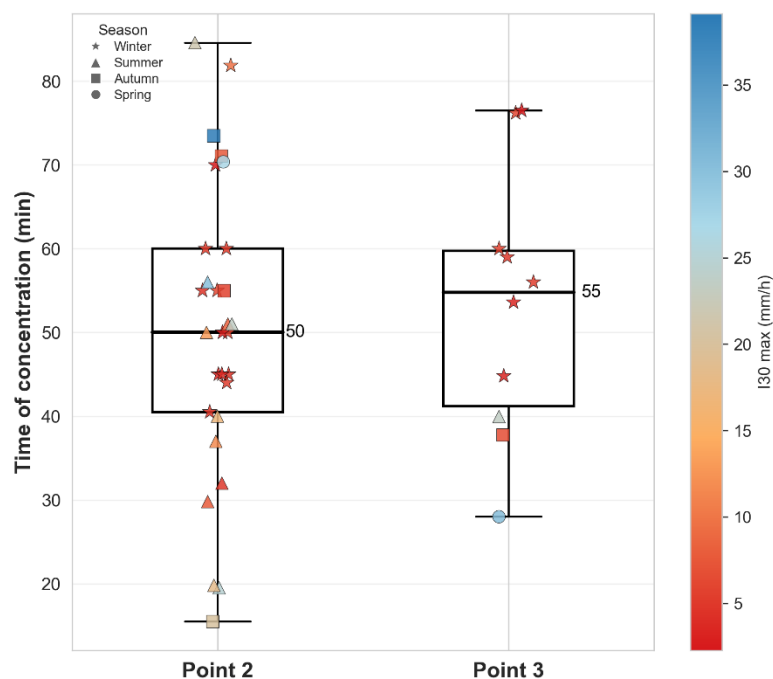
3.2.1 Estimating flow travel time

495 *Comparison of time of concentration methods*

As illustrated in Fig. 5, the response times for the two nested sub-catchments are remarkably similar, with median values of
50 and 55 minutes for Point 2 (84 ha) and Point 3 (111 ha), respectively. Given the 400 m channel distance separating these
two outlets, this 5-minute median delay translates to an average flow velocity of approximately 1.33 m s^{-1} , a realistic value for
channel routing. However, T_c exhibits substantial inter-event fluctuation, ranging from roughly 15 to 85 minutes. Point 2
500 displays a wider dispersion, primarily because its dataset encompasses a broader variety of seasonal configurations and rainfall
intensities, whereas the usable events for Point 3 are characterized by greater meteorological and seasonal homogeneity.
The high standard deviation observed across events reflects the strong sensitivity of the catchment to dynamic variables,
including rainfall intensity, spatial distribution of rainfall, and antecedent soil moisture. Statistically, the 5-day antecedent
precipitation is the only factor showing a significant correlation with observed response times ($\rho = -0.33^*$). This negative
505 correlation indicates that wetter initial conditions tend to shorten the concentration time. This variability aligns with the
findings of Langridge *et al.* (2020) based on an analysis of 1,400 flood events in the UK. They demonstrated that high-intensity



rainfall on saturated soils triggers a rapid hydrological response, whereas moderate rainfall on dry soils significantly elongates the time of concentration. These observations suggest that characterizing the basin's response with a single, constant T_c parameter is physically limiting, highlighting the need for dynamic estimation methods.



510

Figure 5. Comparative boxplots of observed concentration times at point 2 (84 ha) and point 3 (111 ha). Individual events are shown as markers, distinguished by season (symbol shape) and maximum 30-min rainfall intensity (I30max; colour gradient). Numerical median values are indicated.

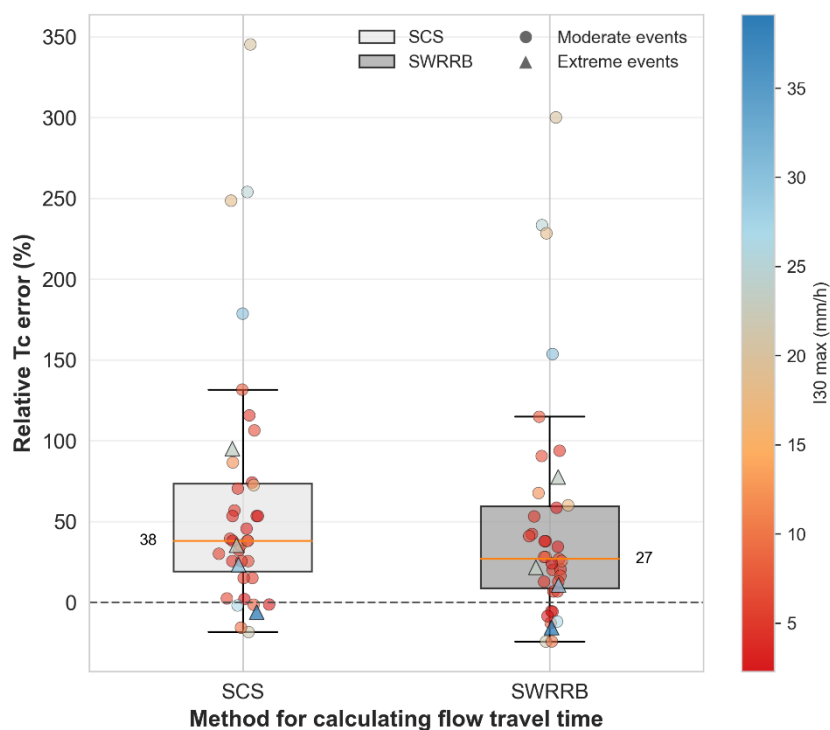
Contrasting with this observed dynamism, the simulated travel time along the longest hydraulic path exhibits minimal variation across the 2014–2024 period. For both empirical methods (SCS velocity and SWRRB), inter-annual standard deviations remain below 1 minute. Despite annual updates to the agricultural land use maps (SIGEC), the modelled hydraulic response remains static, which can be explained by the limited discretisation of roughness parameters. Assigning Manning's coefficients to broad categories like "arable land" fails to distinguish between specific crop types, or the seasonal evolution of the canopy, thereby masking the actual hydraulic impact of the changing vegetation cover.

Temporal dynamics are poorly reproduced by both methods, which exhibit a persistent bias toward overestimating travel times. While median errors remain at 27% for SWRRB and 38% for SCS, maximum relative errors escalate to 300% and 350%, respectively (Fig. 6). These severe overestimations corroborate the observations of Grimaldi *et al.* (2012), who highlighted that static empirical formulas inherently produce very large uncertainties, often exceeding hundreds of percent, when applied to dynamic catchments. Although the SWRRB approach is significantly less biased than the SCS velocity method, both remain fundamentally limited. This is evidenced by a significant positive correlation between the relative T_c error and antecedent moisture ($\rho = 0.34^*$). Because static models fail to capture the fact that larger runoff volumes—generated under wetter

525



antecedent conditions—produce deeper and faster flows, their overestimation of travel times is systematically exacerbated as soil saturation increases. Consequently, accurate flow routing in agricultural catchments demands dynamic parameterization rather than rigid topographic equations.



530

Figure 6. Distribution of relative errors (%) in time of concentration (T_c) estimation comparing the SCS velocity and SWRRB methods. Data points represent individual rainfall-runoff events ($n = 39$), with the colour gradient indicating the maximum 30-minute rainfall intensity. Numeric median values are displayed.

Spatial travel time patterns

535 Visually, the two methods generate different spatial patterns (Fig. 7). The SCS method yields a diffuse travel time map with smooth gradients and a less sharply defined dendritic network. This smooth spatial gradient stems directly from the method's distributed architecture, which relies on a cumulative, pixel-by-pixel summation. However, while this cumulative approach captures landscape heterogeneity, it introduces a high sensitivity to DEM micro-topography. A single pixel with a near-zero slope or high roughness acts as a hydraulic bottleneck, disproportionately inflating the accumulated travel time for the entire upstream contributing area. This structural flaw explains the systematic overestimation of T_c by the SCS method (Median error = 38%; Fig. 6).

540

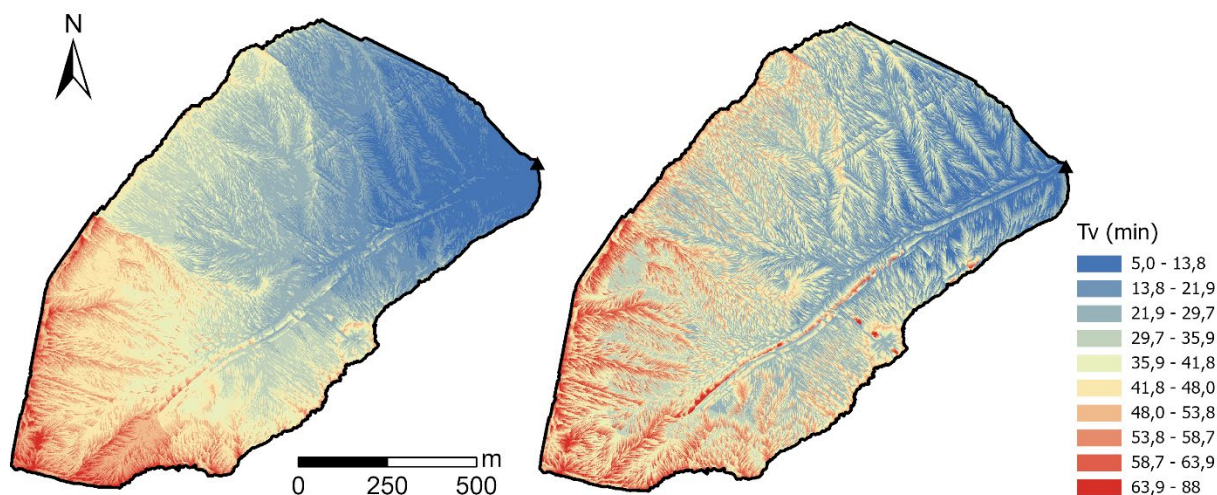


Figure 7. Spatial patterns of flow travel time (T_v) to the outlet calculated using the SCS velocity method (left) and the SWRRB method (right) for the year 2021 in the 111 ha basin (Point 3).

545 Conversely, the SWRRB method clearly delineates the network's dendritic structure with highly contrasted boundaries (Fig. 7, right). Unlike the cumulative SCS approach, SWRRB calculates the travel time for each cell based on path-averaged hydraulic parameters (slope, Manning's n) computed over distinct routing phases. Consequently, the sharp spatial gradients observed on the map do not reflect sensitivity to micro-topography, but rather mark the abrupt transitions between different flow regimes. Within a given flow type, the path-averaging technique acts as a spatial low-pass filter. Although this inherent smoothing may
 550 overlook small-scale hillslope retention features, it provides critical robustness against single-pixel DEM noise. The resulting map reveals structured preferential flow paths extending further upstream, ultimately producing a lower global T_c that better approximates the observed catchment dynamics (median error = 27%; Fig. 6).

Limitations and sensitivity to scale

The SCS velocity method relies on empirical contributing area thresholds to proxy open channel initiation. While specifically
 555 calibrated for the Chastre catchment, relying solely on fixed drainage areas limits the method's transferability, as the transition to channelized flow is governed by complex geomorphological processes. To overcome this site-specificity, future frameworks could integrate more advanced channel initiation criteria. These include foundational slope-area thresholds (Montgomery and Dietrich, 1988), probabilistic approaches (Istanbulluoglu et al., 2002), and topographic metrics for gully development (Torri and Poesen, 2014; Wang et al., 2022). Incorporating such physically based criteria would refine automated flow regime
 560 classification and greatly enhance spatial transferability.

While the comparison of methods highlights the relative robustness of SWRRB method against micro-topographic noise, the interpretation of these results requires caution regarding the definition of T_c itself. Theoretically restricted to the longest hydraulic path, T_c reduces a distributed two-dimensional process to a one-dimensional metric. By ignoring the spatial variance of contributing areas, it characterizes a maximum potential travel time rather than the effective mean response of the basin.



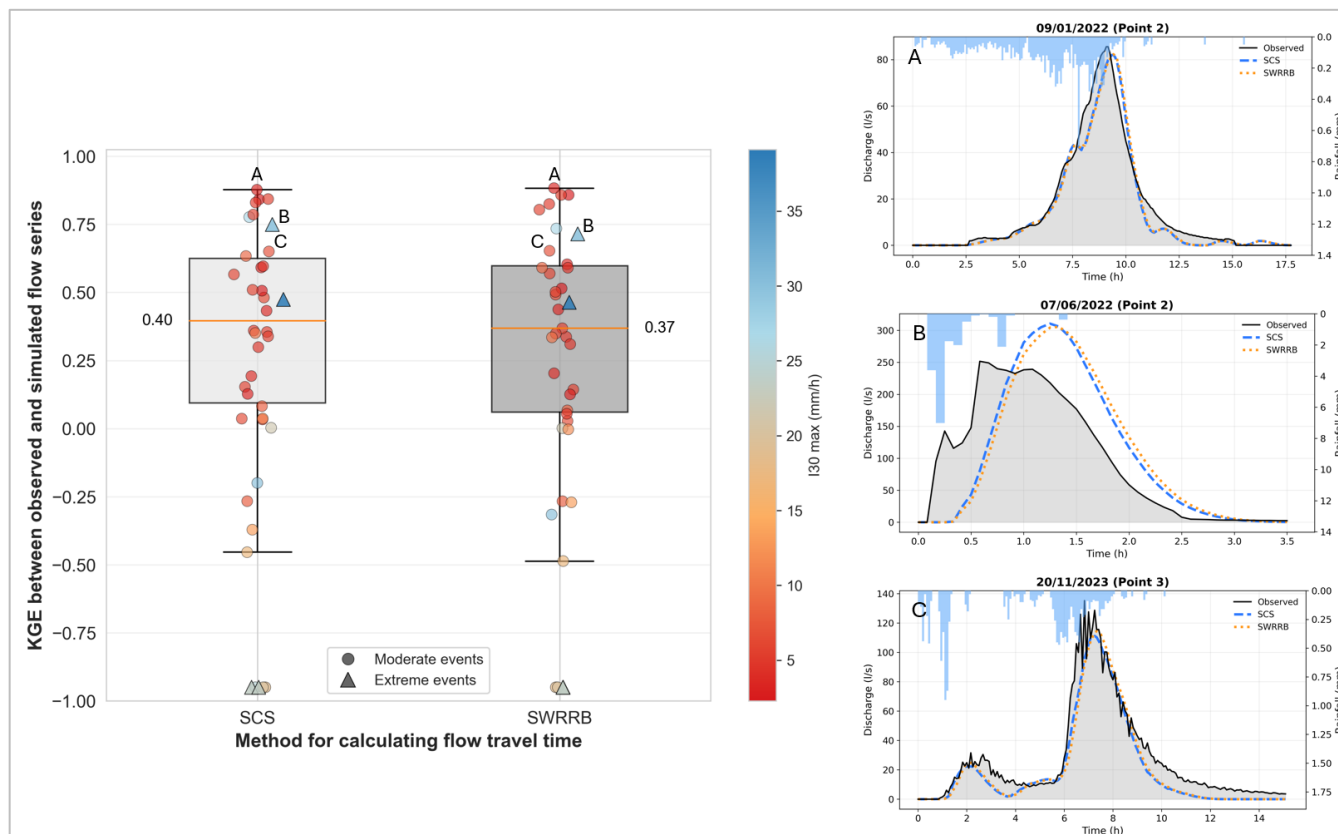
565 Furthermore, the observed T_c is subject to methodological interpretation. Determining the cessation of surface runoff via the inflection point on the recession limb remains a partly subjective process, sensitive to hydrograph noise (Grimaldi et al., 2010; McCuen, 2009). This confirms that the calculated error margins (Fig. 6) inevitably include both modelling bias and observational uncertainty.

570 Finally, the systematic overestimation of T_c is a direct consequence of utilizing a high-resolution (1 m) DEM. While such precision is highly desirable for accurately delineating realistic spatial flow networks, it explicitly captures micro-topographic sinuosity, which structurally elongates the flow paths (Murphy et al., 2008; Veeck et al., 2020). This geometric tortuosity inherently inflates calculated travel times, particularly along the catchment's longest flow path (Grimaldi et al., 2012; Moglen and Hartman, 2001). However, this localized delay at the catchment's most remote boundaries does not necessarily reflect poor global routing efficiency. Because T_c relies on an extreme boundary value, it is insufficient as a standalone metric to validate
575 the model's overall flow propagation. A robust evaluation must therefore cross-reference T_c with the integrated catchment response.

3.2.2 Hydrograph estimation and routing performance

Having assessed the runoff generation capacity, this section extends the validation to the full hydrograph analysis. To isolate the specific performance of the routing algorithms (SCS vs. SWRRB), the excess rainfall was generated using the Jain method,
580 identified as the most robust volumetric approach in Sect. 3.1.

The comparative analysis of hydrograph simulations reveals a remarkable convergence between the two routing strategies (Fig. 8). Despite structural differences in T_c estimations, global performance metrics are statistically equivalent, with median KGE values of 0.40 (SCS) and 0.37 (SWRRB). This suggests that hydrograph morphology is governed primarily by the temporal distribution of rainfall intensity rather than the sensitivity of routing parameters. The mean difference in calculated
585 T_c between the two methods (~ 7 min) is negligible relative to the typical duration of the rainfall events observed in this dataset. Furthermore, this deviation corresponds to barely more than a single computation time-step ($\Delta t = 5$ min). Therefore, the specific damping effect of the routing algorithm is insufficient to significantly alter the signal imposed by the hyetograph. This dominance of rainfall temporal variability over catchment routing is characteristic of small headwater basins where the flow travel time is short compared to the storm duration (Merz and Blöschl, 2003; Viglione et al., 2010).



590 **Figure 8.** Distribution of KGE between observed and simulated flows by Hidropixel for the SCS and SWRRB methods (left-hand
 panel). Each dot represents a single rainfall-runoff event ($n = 39$). Marker shapes distinguish event categories (circles for normal
 events, triangles for extreme events), while the colour gradient indicates the maximum 30-minute rainfall intensity. The lower bound
 of the y-axis is fixed at -1 to avoid displaying extreme negative values. The right-hand panels present representative hydrographs
 595 illustrating the model's performance at point 2 under (A) moderate rainfall conditions ($KGE = 0.88$) and (B) extreme rainfall
 conditions ($KGE = 0.73$), as well as its performance at point 3 ($KGE = 0.65$).

A Spearman rank correlation analysis between the efficiency metric (KGE) and key hydro-meteorological descriptors reveals
 distinctly regime-dependent performance. Model skill exhibits a significant positive correlation with rainfall duration
 ($\rho = 0.40^*$), but a highly significant negative correlation with maximum rainfall intensity ($I30\ max, \rho = -0.46^{**}$). Total rainfall
 depth shows no significant influence. Consequently, acceptable hydrograph restitution (positive KGE) is primarily achieved
 600 during prolonged, lower-intensity rainfall events, whereas severe model failures coincide with short-duration, high-intensity
 storms. These results again highlight that the static SCS-CN framework, empirically calibrated for 24-hour events, lacks the
 temporal resolution to capture rapid Hortonian runoff processes.

To further dissect the model's routing behaviour, the relative errors for Q_p , T_p and T_b were analysed for both routing methods.
 The results confirm the statistical similarity between the SCS and SWRRB methods, with both exhibiting identical error
 605 patterns and median values (Fig. 9).



Regarding peak discharge, the analysis shows no systematic bias (median relative errors of -7% to -9%), but reveals pronounced dispersion (Fig. 9). Extreme events display very large positive deviations, frequently exceeding 100%, confirming that Q_p errors are heavily dominated by high-intensity storms. However, discharge observations during such high-magnitude floods are inherently subject to substantial uncertainty due to extreme flows reaching the hydraulic and operational limits of the in situ measurement infrastructure. Beyond these observational limits, this volatility is consistent with the mechanical propagation of the volumetric uncertainties discussed in Sect. 3.1, where the production module's threshold behaviour triggers disproportionate peak responses once the abstraction is exceeded (Walega et al., 2020).

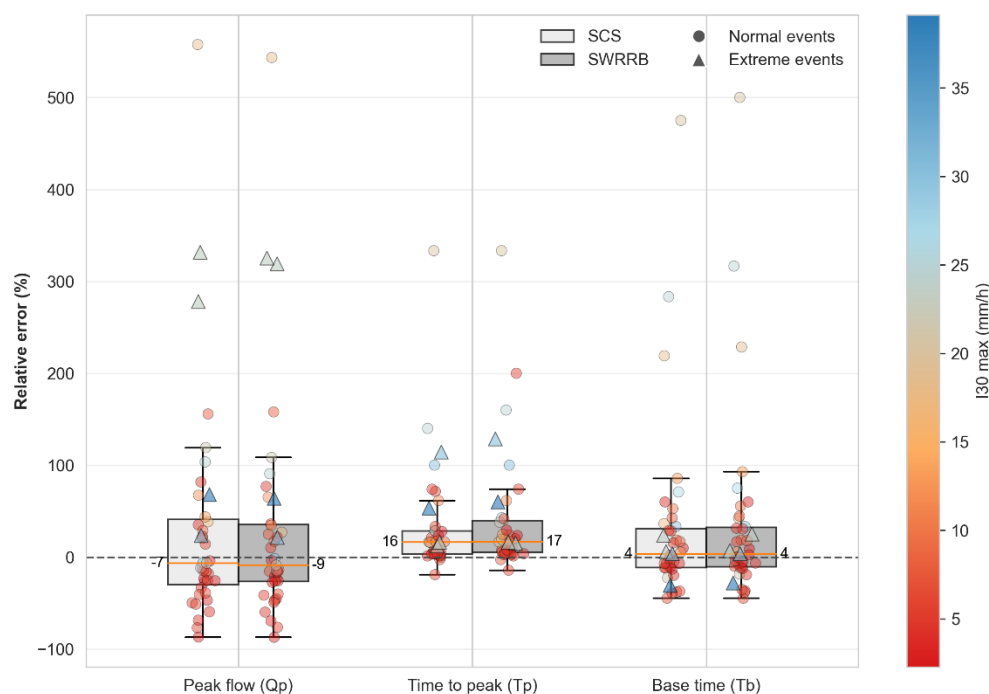


Figure 9. Relative errors (%) of hydrological flood indicators for events (based on Jain's method to estimate runoff volume). The boxes compare Hidropixel SCS and SWRRB for peak flow (Q_p), peak time (T_p), and base time (T_b). Marker shapes distinguish event categories (circles for normal events, triangles for extreme events), while the colour gradient indicates the maximum 30-minute rainfall intensity. Median values are indicated on each boxplot.

The overwhelming sensitivity of Q_p to CN parameterization compared to routing variables (e.g., T_c) is well-documented (Banasik et al., 2016; Mishra and Singh, 2003; Moghadasi et al., 2018; Ponce and Hawkins, 1996; Vojtek et al., 2019). Rather than undermining the value of distributed routing, this structural sensitivity highlights critical pathways for future research. To fully leverage high-resolution frameworks like Hidropixel, there is an urgent need to transition from static CN tables toward dynamic, continuous soil moisture accounting. Integrating satellite-derived antecedent moisture or radar-based infiltration modelling would allow the precision of the 1-m hydraulic routing to be matched by a similarly refined production module, finally overcoming the "all-or-nothing" threshold behaviour of the classical framework.



625 The most critical finding of this temporal analysis, however, lies in the synchronization of the runoff window. While the model exhibits a consistent delay in time to peak—with median overestimations of +16% (SCS) and +17% (SWRRB) due to the high-resolution 1-m DEM tortuosity—the base time errors remain centred near zero (4%). This demonstrates that the observed and simulated runoff windows coincide effectively, confirming that the routing architecture is structurally robust. Consequently, the model correctly captures the overall duration of the hydrological response; any observed narrowing or
630 widening of the hydrograph is better interpreted as a secondary consequence of volumetric deviations (Sect. 3.1) rather than a structural deficiency in transfer timing. This stable temporal envelope underscores the model's reliability for characterizing flood dynamics in ungauged agricultural landscapes.

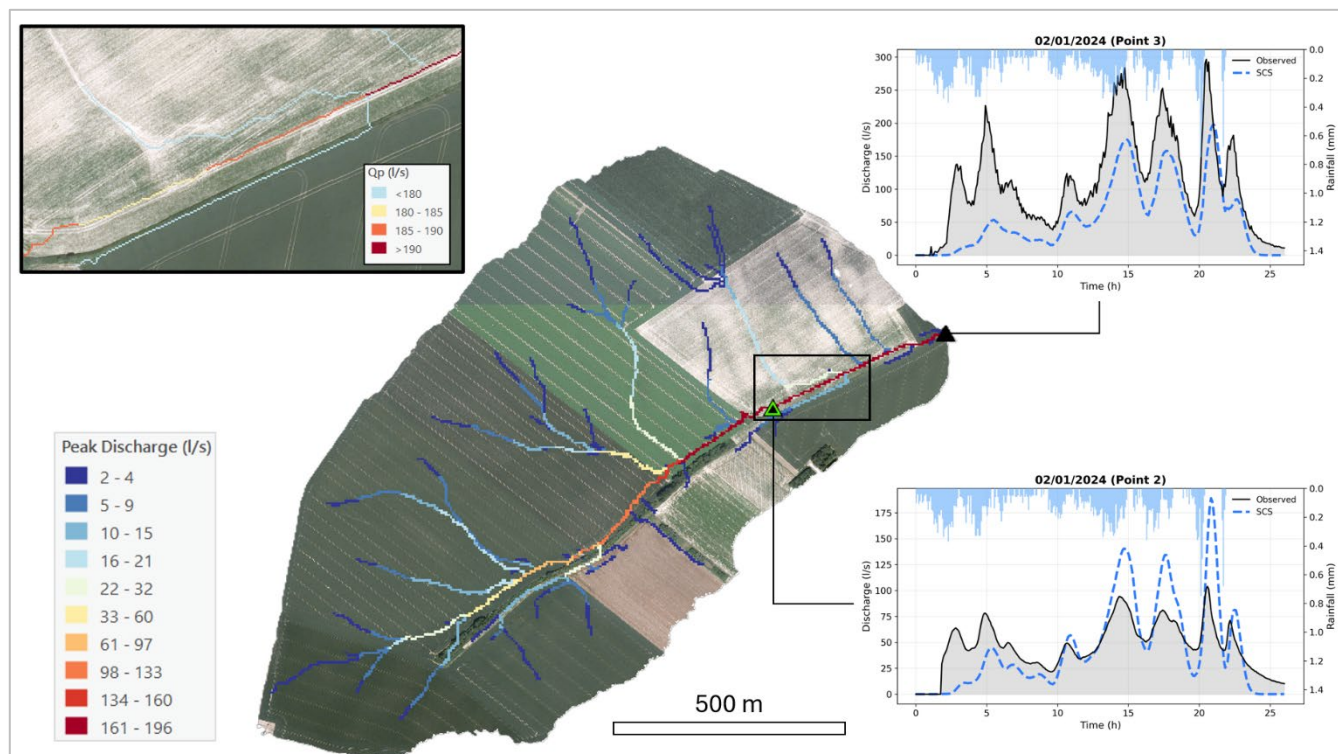
Consequently, the selection between the SCS and SWRRB methods should be guided primarily by the specific modelling objective rather than raw predictive efficiency. The SCS velocity method offers superior spatial discretization, explicitly
635 representing landscape heterogeneity; this makes it particularly effective for assessing the impact of localized land-use features (e.g., specific crop allocations or buffer strips). However, this high resolution renders it inherently susceptible to local DEM artifacts and grid-size dependencies, potentially necessitating targeted spatial calibration. Conversely, the SWRRB approach relies on a simpler, averaged classification of flow regimes. This averaging acts as a spatial low-pass filter, making the method significantly more robust against topographic noise and easier to implement *a priori*, but at the inevitable cost of smoothing
640 out fine-scale spatial heterogeneity along the flow paths. In essence, the structural strengths of one method perfectly mirror the inherent weaknesses of the other.

3.3 Flood hazard assessment

Building upon the comparative analyses, this final section operationalises a spatially distributed flood hazard assessment. Based on the efficiency criteria established in Sect. 3.1 and 3.2, the optimal configuration combines the Jain-adjusted CN
645 method with the Hidropixel distributed SCS routing to explicitly account for landscape heterogeneity. By iteratively computing the peak discharge for every pixel along the concentrated flow paths, this framework directly translates the hydrological model into a continuous, high-resolution hazard map of the drainage network.

3.3.1 Application to an observed rainfall event

To illustrate the spatial consistency and operational potential of the proposed framework, the model is applied to a multi-modal
650 rainfall event (January 2, 2024; duration: 18 h, total depth: 28 mm). Figure 10 demonstrates the model's capacity to propagate runoff dynamically throughout the catchment using high-resolution topographic data. An accompanying animation of discharge rates (Supplement, Video S1) further emphasizes the framework's capability for operational risk management. Complementary analyses and further validation examples across diverse rainfall profiles are available in the appendices (Fig. D1, D2 and E1).



655

Figure 10. Spatial distribution of simulated peak flow using the SCS velocity method along the concentrated flow paths of the catchment during the 02/01/2024 rainfall event (duration: 18 h, total depth: 28 mm). The right panels display the corresponding hydrographs at the upstream (Point 2) and downstream (Point 3) monitoring stations, comparing observed discharge with the model outputs using both the SCS and SWRRB routing configurations. The zoomed area highlights the spatial variability of Q_p . Maps data: © Service public de Wallonie, 2018.

660

As highlighted in the magnified inset, the model effectively captures two hydrodynamic behaviours that dictate the spatial variability of peak flows. First, on gentle slopes where the contributing area increases slowly, the hydrograph tends to broaden and its peak attenuates. Because low gradients significantly reduce flow velocity, runoff generated across the landscape converges locally over an extended period (Paiva and Lima, 2024; Woltemade and Potter, 1994).

665

Conversely, where landscape morphology forces flow paths to rapidly converge, local peak amplification occurs. In these areas, lateral runoff inputs arrive simultaneously (in-phase). Because discharge scales non-linearly with the contributing area (power law), this rapid synchronization and overlapping of flows drastically reduces overall travel times, yielding disproportionately large flood peaks (Ayalew et al., 2014; Bracken and Croke, 2007; Ogden and Dawdy, 2003). This spatial heterogeneity in routing behaviour explains why hydrograph peaks do not always scale monotonically downstream: attenuation dominates over gentle, unconnected reaches, whereas amplification appears where connectivity and drainage area increase.

670

The accompanying hydrographs at Point 2 and Point 3 confirm the method's ability to reproduce complex, multi-peak catchment responses (Fig. 10). Both the SCS and SWRRB models successfully capture the timing and magnitude of the primary peaks generated by the rainfall bursts later in the event. However, a noticeable discrepancy occurs during the initial



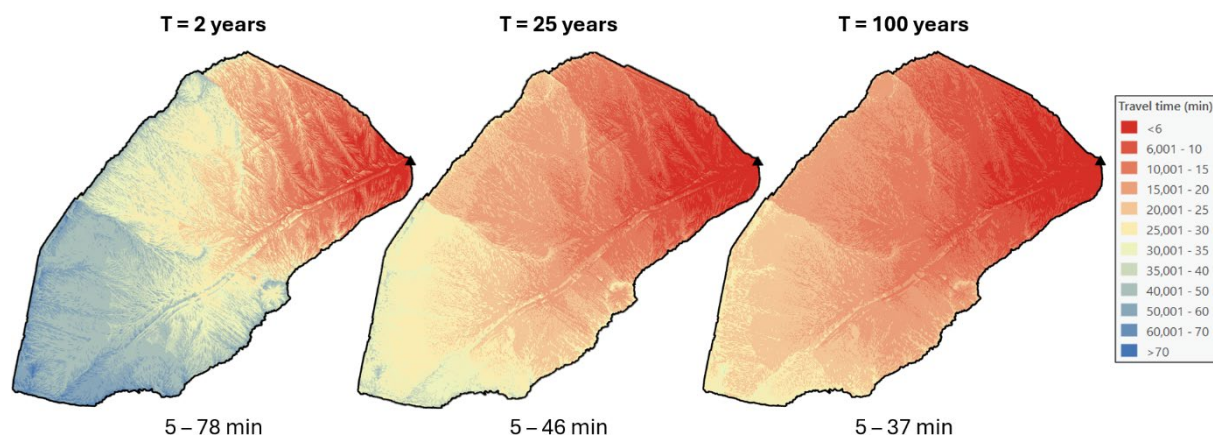
hours (3 to 6 h), where the model completely misses the first observed runoff peak. This physically illustrates the structural
 675 limitation of the static initial abstraction threshold discussed previously.

Ultimately, this application demonstrates the substantial potential of coupling a distributed volumetric approach (adjusted
 SCS-CN) with high-resolution topographic routing (Hidropixel) in ungauged agricultural areas. The framework successfully
 delivers a spatially explicit, first-order quantification of pluvial flood hazards without requiring extensive parameter
 680 calibration. Nevertheless, to further bridge the predictive gap, future evolutions of the tool must address the rigid threshold
 behaviour of the runoff generation module. Furthermore, coupling these conceptual estimates with machine learning or
 regionalization in hybrid frameworks offers a promising avenue for transferring hydrological behaviour from gauged to
 ungauged catchments (Prakash et al., 2025).

3.3.2 Application to extreme design rainfall scenarios

In the absence of observational data for such rare magnitudes, the application to extreme meteorological forcing (25-year and
 685 100-year return period design storms) must be interpreted as an exploratory scenario analysis rather than a validated prediction.
 This approach demonstrates the framework's capacity to delineate flood-prone corridors and evaluate how flow propagation
 accelerates under exceptional rainfall in ungauged agricultural catchments. The model was applied to two synthetic extreme
 rainfall scenarios: a 25-year and a 100-year return period design storm.

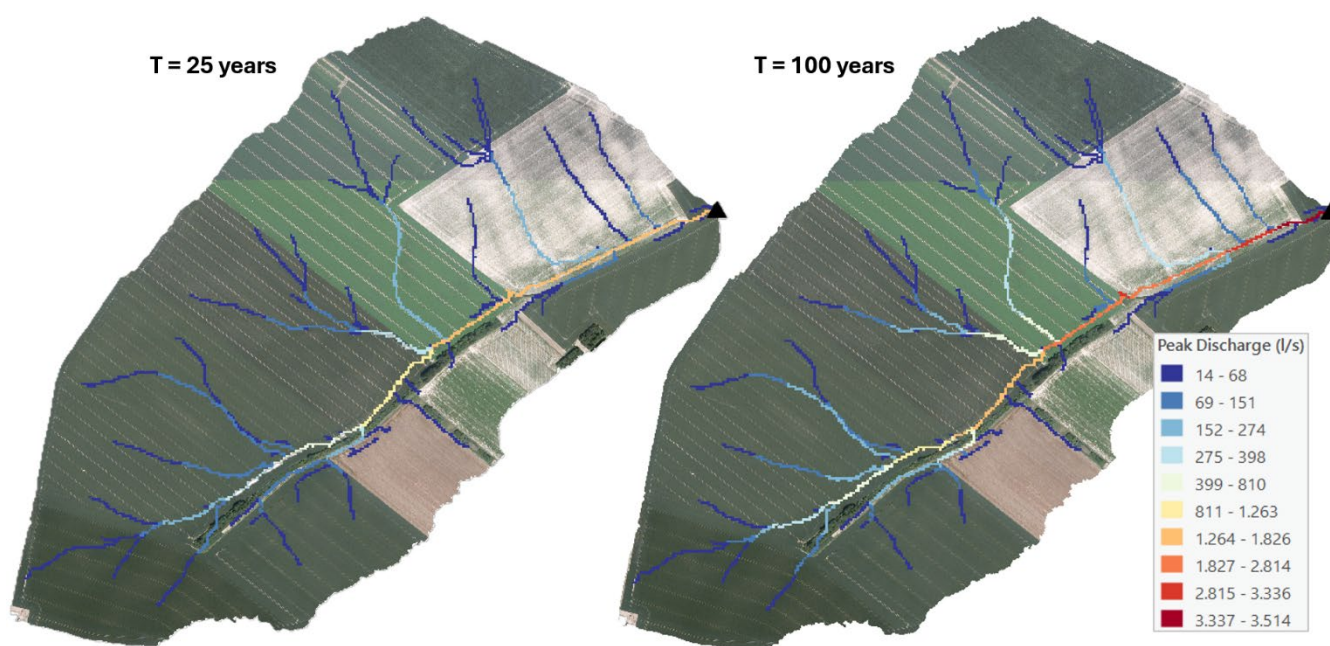
By applying Meyersohn's equation (Eq. 14) to adjust pixel-level travel times according to extreme rainfall intensities, the
 690 model captures a drastic shift in the spatial distribution of travel times (Fig. 11). During a standard 2-year event, the maximum
 travel time reaches 78 minutes, whereas it decreases to 46 minutes and 37 minutes under the 25-year and 100-year scenarios,
 respectively. This simulated reduction is conceptually consistent with the expected physical hydrological behaviour of extreme
 events, where greater runoff volumes generate deeper flows that significantly increase hydraulic efficiency and flow velocities.



695 **Figure 11. Spatial distribution of runoff travel times across the catchment under varying design storm magnitudes (2-year, 25-year, and 100-year return periods) adjusted according to Meyersohn's formula.**



700 A spatial comparison of simulated peak flows between the 25-year and 100-year design storms reveals a pronounced amplification of flow magnitude along the main concentrated flow path (Fig. 12). While peak discharges increase substantially—nearly doubling at the main outlet from approximately $1,826 \text{ l s}^{-1}$ ($T=25$ years) to $3,514 \text{ l s}^{-1}$ ($T=100$ years)—this relative amplification is highly spatially heterogeneous. The percentage increase in peak flow systematically escalates as flow paths converge, rising from moderate values in the headwaters (30-50%) to a maximum exceeding 90% in the main thalweg. This localized intensification indicates that flood severity under extreme forcing is primarily driven by enhanced routing efficiency and the rapid, non-linear synchronization of upstream contributions.



705 **Figure 12. Spatial distribution of simulated peak flows along concentrated flow paths for the 25-year and 100-year design storms. Maps data: © Service public de Wallonie, 2018.**

710 Characterizing flood hazard solely through the spatial distribution of Q_p presents inherent limitations, as it omits the explicit temporal dynamics of the flood wave (e.g., rate of rise, duration of inundation). However, Q_p remains a highly pertinent primary indicator for ungauged catchments (Blöschl, 2013; Prakash et al., 2025). Because peak discharge mathematically integrates both the total volume of excess runoff and the geomorphological convergence of flow paths, it effectively captures the maximum hydraulic stress exerted on the landscape and infrastructure.

4 Summary & Conclusions

This study evaluated a high-resolution, spatially distributed hydrological framework designed to assess pluvial flood hazards in ungauged agricultural catchments. By systematically decoupling the runoff generation and routing phases, the analysis



715 provided critical insights into the physical capabilities and structural limitations of conceptual modelling in ungauged environments.

The foundation of this framework relies on an accurate estimation of effective runoff. While the Jain method significantly reduces volumetric bias compared to the traditional SCS-CN approach, our findings highlight the overarching dominance of rainfall intensity over total depth in small, fast-responding catchments. The distinctly regime-dependent performance—where
720 the model struggles to capture rapid, infiltration-excess (Hortonian) runoff during high-intensity storms—confirms the structural rigidity of the static CN framework. To overcome this limitation, future conceptual frameworks must transition toward continuous soil moisture accounting rather than relying on static, event-based thresholds.

Regarding hydraulic transfer, the comparative analysis of routing algorithms revealed that the choice between velocity-based (SCS) and path-averaged (SWRRB) routing schemes yields only marginal differences in global hydrograph restitution. The
725 routing phase acts primarily as a mechanical propagator of volumetric uncertainty. Thus, while peak magnitude remains highly sensitive to these input variations, the routing framework consistently reproduces the overall runoff window reasonably well, maintaining base time errors centred near zero. By shifting the focus from a single outlet to a continuous drainage profile at a 1-m resolution, the model successfully captured the complex interplay between hydrodynamic attenuation along low-gradient reaches and the non-linear, kinematic synchronization of peak flows at tributary confluences.

730 These spatially distributed insights are particularly valuable for proactive risk management. The application of the model to extreme design storms (25-year and 100-year return periods) demonstrated how the active flow network dynamically expands, with peak discharges escalating by over 90% along the main thalweg due to rapid flow path synchronization. Consequently, this framework serves as a valuable tool for risk-informed land management, enabling stakeholders to explicitly identify hotspots most susceptible to extreme flows.

735 Moving forward, the primary limitation of this framework lies in its validation within a single temperate context. Since runoff partitioning is highly sensitive to local pedological and climatic conditions, future research must prioritize the systematic testing of this coupled approach (Jain-adjusted CN and Hidropixel routing) across contrasting environments. Evaluating the model's robustness across diverse topographic gradients and soil types will be essential to establish generalized and reliable guidelines for ungauged catchments. However, technical refinement alone is insufficient; addressing the ungauged challenge
740 requires a fundamental commitment to expanded field monitoring and open-access data sharing. Ultimately, as extreme, short-duration storms become increasingly frequent under a changing climate, refining these spatially distributed, uncalibrated tools will be critical to support proactive land management and mitigate flood risks in vulnerable landscapes globally.

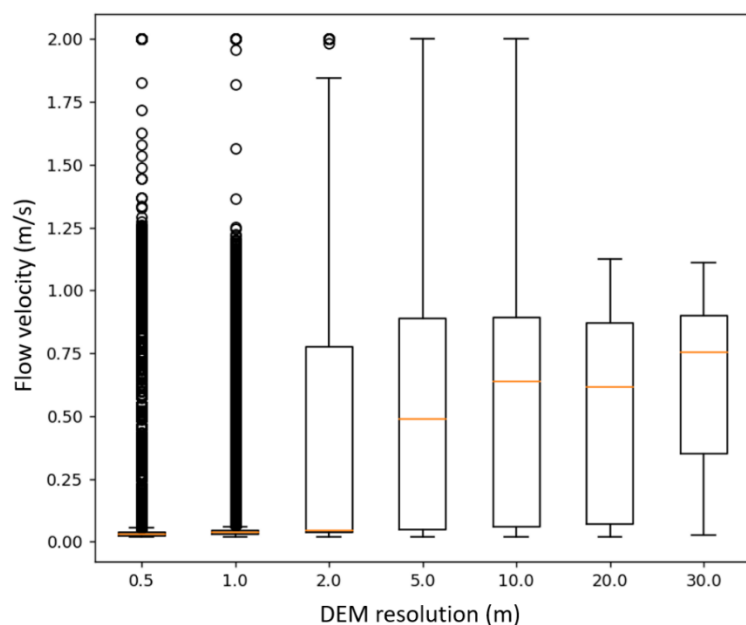
745



Appendices

Appendix A. Travel time analyses

750 Figure A1 illustrates the sensitivity of spatially distributed local flow velocities to DEM resolution. At high resolutions, a
larger proportion of the catchment is characterized by sheet flow, resulting in lower local velocities. Conversely, coarser
resolutions tend to artificially accelerate flow concentration, significantly reducing the frequency of sheet flow pixels. This
highlights the necessity of implementing a minimum slope threshold to prevent local travel times from reaching physically
unrealistic values in nearly flat terrain. A threshold of 0.5% was selected for this study, as it yields Time of concentration (T_c)
755 estimates that are consistent in order of magnitude with both the Mockus (1961) lag equation and direct hydrograph
observations (Sect. 2.3.2).



760 **Figure A1. Impact of spatial resolution on local water velocity estimates calculated via the SCS velocity method in the 84 ha catchment. Orange lines represent median values for each resolution.**



Appendix B. Hydrological data

765 **Table B1. Characteristics of selected rainfall-runoff events for the Chastre catchment (Points 2 and 3).**

Point	Event	Date	Rainfall		Direct runoff			Runoff coefficient*	Return period (years)
			Total rainfall depth (mm)	Duration (h)	Excess rainfall (mm)	Peak discharge (l/s)	Time-to-peak (h)		
Moderate events									
2	1	21-09-14	11.8	3.2	0.35	39	3.1	0.03	
2	2	03-01-15	14.6	6.8	1.18	163	6.1	0.08	
2	3	08-01-15	19.8	5.9	2.81	175	5.9	0.14	
2	4	10-01-15	5.2	2.3	0.43	54	2.1	0.08	
2	5	05-06-15	18.6	1.9	0.86	160	1.8	0.05	
2	6	30-01-16	15.2	9.2	0.97	67	8.0	0.06	
2	7	10-06-19	12.4	0.5	0.14	97	0.4	0.01	
2	8	18-08-19	25.0	5.2	0.31	70	4.0	0.01	
2	9	18-06-21	14.4	2.6	0.43	171	2.6	0.03	
2	10	29-06-21	14.1	4.6	0.52	105	2.8	0.04	
2	11	30-06-21	22.0	6.4	2.10	177	3.1	0.10	
2	12	04-01-22	6.0	3.2	0.41	31	1.9	0.07	
2	13	09-01-22	13.9	9.9	1.16	86	9.1	0.08	
2	14	20-02-22	7.0	2.3	0.19	53	2.5	0.03	
2	15	20-05-22	14.1	1.6	1.16	263	1.2	0.08	
2	16	08-06-22	14.7	6.5	1.11	118	4.5	0.08	
2	17	23-07-23	7.2	0.8	0.10	48	1.0	0.01	
2	18	05-12-23	13.3	9.6	0.92	89	7.6	0.07	
2	19	10-12-23	4.4	1.9	0.22	31	1.0	0.05	
2	20	19-12-23	10.3	9.7	0.91	39	5.7	0.09	
2	21	02-01-24	27.9	18.2	5.10	104	20.6	0.18	
2	22	21-06-24	12.1	1.8	0.46	79	1.1	0.04	
2	23	07-09-24	10.1	0.5	0.10	156	0.3	0.01	
2	24	19-11-24	18.7	8.1	1.24	110	4.4	0.07	
2	25	06-12-24	3.4	2.1	0.30	47	2.2	0.09	
2	26	22-12-24	2.5	3.0	0.30	57	1.4	0.12	
3	27	28-12-21	6.0	4.7	0.33	36	3.9	0.05	
3	28	04-01-22	6.0	3.2	0.94	96	1.2	0.16	
3	29	09-01-22	13.9	9.9	2.26	192	9.2	0.16	
3	30	20-11-23	13.8	10.2	1.32	135	6.8	0.10	
3	31	05-12-23	13.3	9.6	1.68	240	7.6	0.13	
3	32	10-12-23	4.4	1.9	0.32	48	1.8	0.07	
3	33	19-12-23	10.3	9.7	0.68	48	6.3	0.07	
3	34	02-01-24	27.9	18.2	9.22	297	20.5	0.33	
3	35	04-05-24	18.4	2.2	0.97	376	0.8	0.05	
Extreme events									
2	36	07-06-22	17.9	1.3	1.49	252	0.6	0.08	2
2	37	18-06-24	38.8	7.0	1.37	174	2.6	0.04	10
2	38	08-09-24	21.1	1.6	1.94	319	1.3	0.09	2
3	39	18-06-24	38.8	7.0	1.28	212	2.8	0.03	10

*runoff coefficient = excess rainfall/rainfall



Appendix C. Runoff estimation

770 Van Oost (2003) proposes an adjusted Curve Number (CN) of each grid cell of the drainage area, computing it as a function of crop development and soil crusting stages:

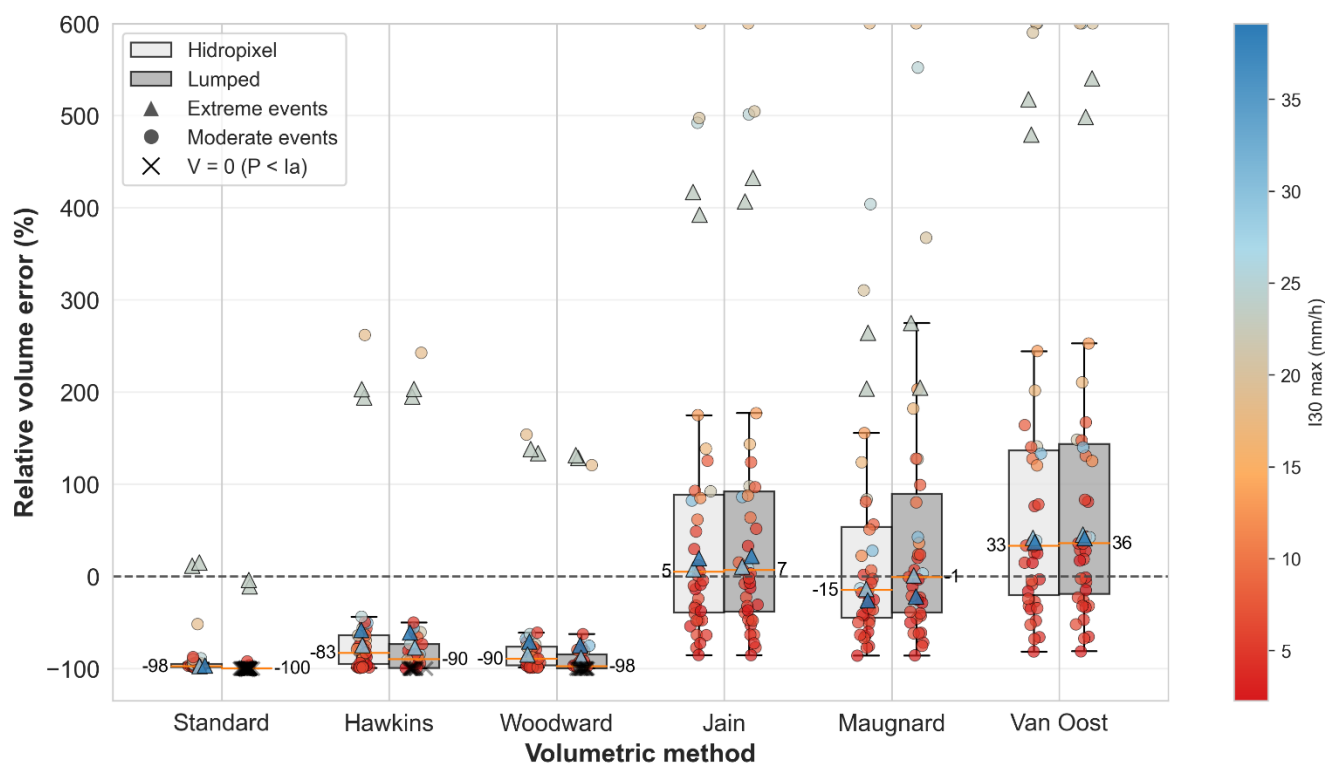
$$CN_{adj} = CN_{max} - \left(\frac{C_c}{100} * c_1\right) + \left(\frac{C_r}{4} * c_2\right) \tag{C1}$$

where CN_{max} represents the maximum theoretical CN derived from the USDA-SCS handbook for specific combinations of cover types and hydrological soil groups typical of Walloon agricultural practices; C_c is the fractional crop cover (%); C_r denotes the soil crusting stage and c_1 and c_2 are coefficients.

775

Subsequently, Maignard (2015) established an empirical relationship via linear regression, demonstrating a significant correlation between the optimal initial abstraction ratio (λ), total rainfall depth (P), and the CN ($R^2 = 0.76$, $NSE = 0.77$, $RMSE = 0.025$, $n=17$):

$$\lambda = -0.01527 - 0.04806 * P + 0.0007609 * P * CN \tag{C2}$$



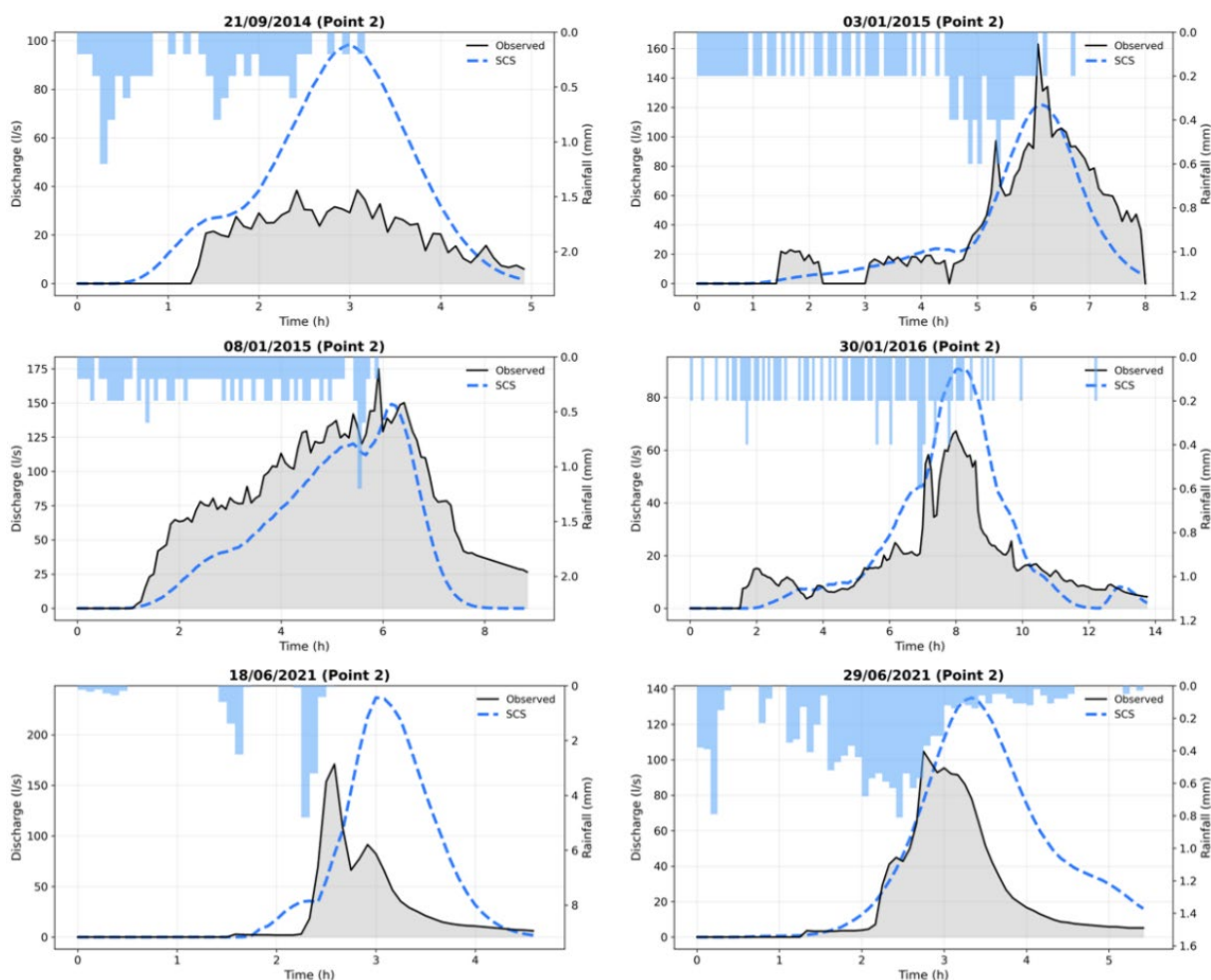
780

Figure C1. Comparative boxplots of signed relative volume error (%) for runoff events ($n = 39$) at the Chastre watershed using the Hidropixel model (light grey) and a lumped model approach (grey). Marker shapes distinguish event categories (circles for normal events, triangles for extreme events), while the colour gradient indicates the 130 max (the maximum intensity of rainfall recorded over a period of 30 minutes), and the black crosses highlight zero-runoff simulations ($P < I_a$). Numeric median values are displayed.



785 To evaluate these dynamic approaches, the Van Oost method for dynamic CN adjustment was coupled with the Jain method
for I_a estimation. As illustrated in Fig. C1, the Van Oost approach does not improve the estimation of runoff volumes. It
introduces a systematic overestimation (median relative errors of +33% and +36%). Conversely, the Maignard method—
which relies on a locally calibrated linear regression to adjust the initial abstraction ratio—demonstrates an improvement,
yielding predictions much closer to the observed volumes. These results underscore that refining the parameter λ through
790 context-specific empirical regressions is a more robust and effective strategy for capturing runoff generation than modifying
the core CN parameter itself.

Appendix D. Hydrograph estimation



795

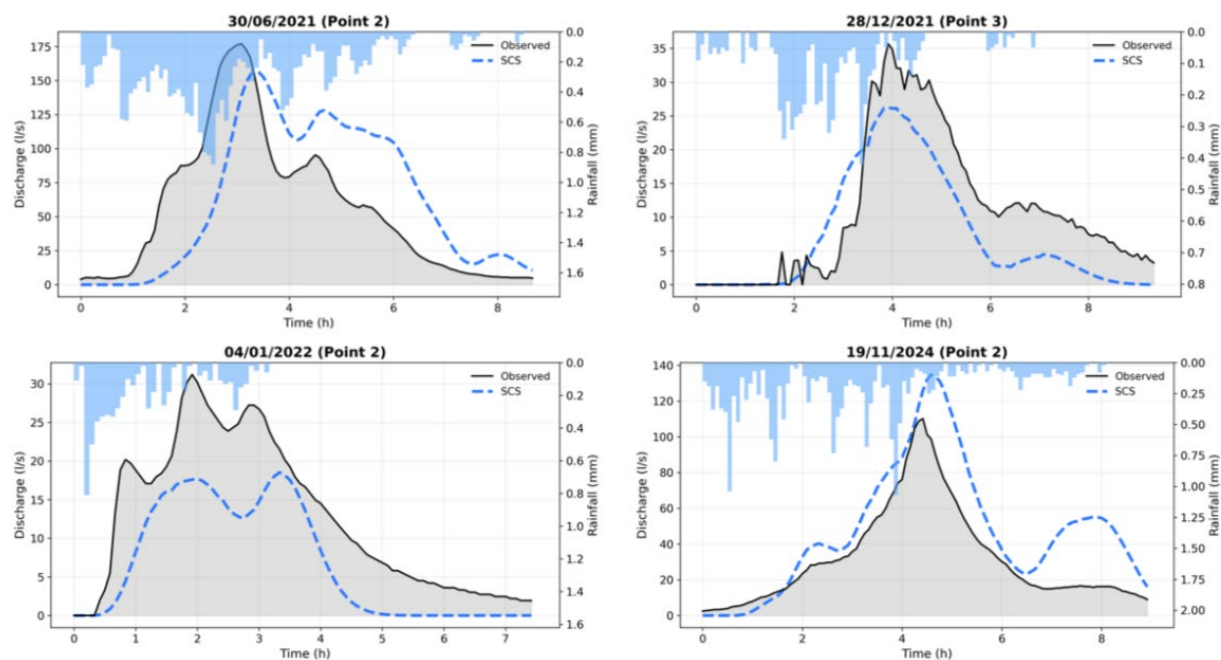
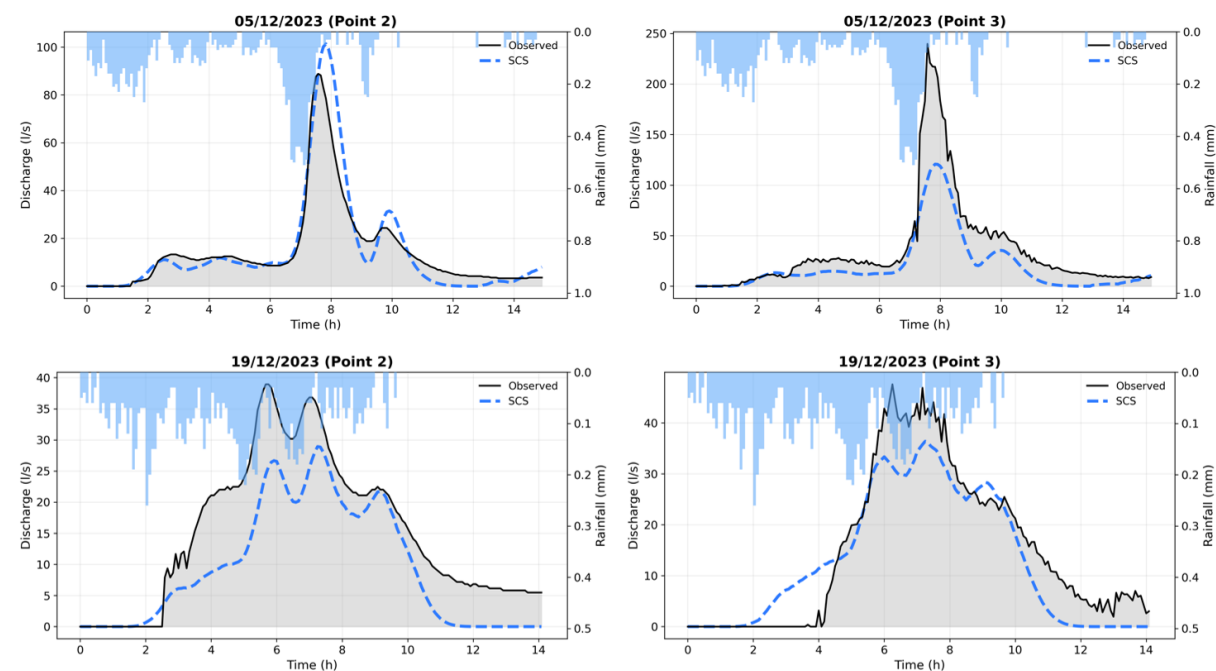


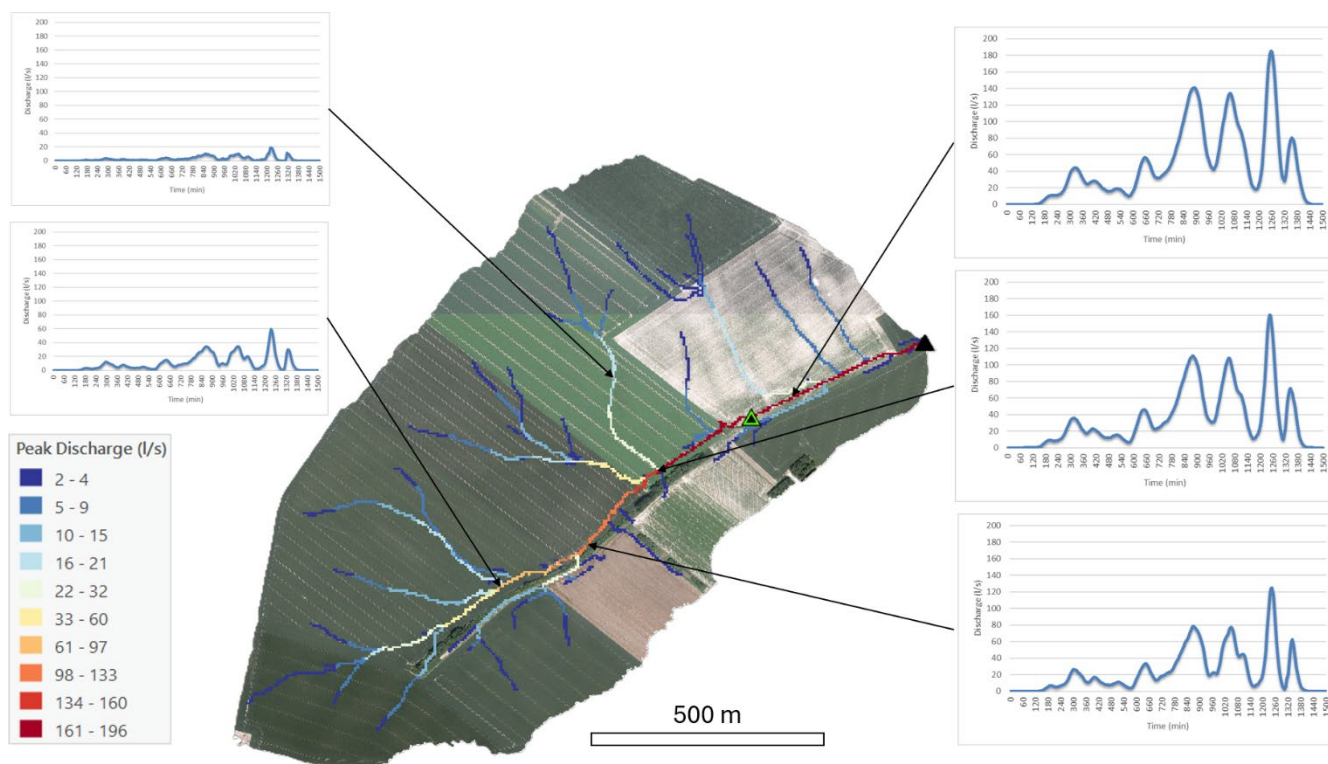
Figure D1. Comparison of observed and simulated hydrographs for a selection of distinct rainfall-runoff events recorded between 2014 and 2024.



800 Figure D2. Simultaneous hydrograph restitution at the upstream (Point 2) and downstream (Point 3) monitoring stations for two rainfall events.



Appendix E. Flood hazard map



805 **Figure E1. Spatio-temporal simulation of the 02/01/2024 runoff event using the Hidropixel SCS model. The central map displays peak discharges ($l\ s^{-1}$) along flow concentration paths, while the surrounding panels show simulated hydrographs at specific locations. The black triangle denotes the main outlet, and the green triangle indicates an upstream gauging station. Maps data: © Service public de Wallonie, 2018.**

810



Code and data availability

The datasets, modelling frameworks, and computational code supporting the conclusions of this manuscript are available from the corresponding author upon reasonable request.

Author contributions

815 Conceptualization, M.H. and A.D.; Methodology, M.H.; Software, M.H. and P.B.; Investigation, G.S.; Data Curation, G.S.; Writing – Original Draft Preparation, M.H.; Writing – Review & Editing, A.D., P.B., and C.B.; Supervision, A.D. All authors have read and agreed to the published version of the manuscript.

Competing interests

The authors declare that they have no conflict of interest.

820 **Acknowledgements**

The research has been funded by the project HYDRAXES, funded by the the Service Public de Wallonie.



References

- 825 Alexopoulos, M. J., Dimitriadis, P., Iliopoulou, T., Bezak, N., Kobold, M., and Koutsoyiannis, D.: Effects of digital elevation model resolution on rain-on-grid simulations: a case study in a Slovenian watershed, *Hydrological Sciences Journal*, 69, 1468–1485, <https://doi.org/10.1080/02626667.2024.2378487>, 2024.
- Arcecent, G. J. and Schneider, V. R.: Guide for selecting Manning’s roughness coefficients for natural channels and flood plains, *Water Supply Paper*, U.S. G.P.O.; For sale by the Books and Open-File Reports Section, U.S. Geological Survey, <https://doi.org/10.3133/wsp2339>, 1989.
- 830 Ayalew, T. B., Krajewski, W. F., Mantilla, R., and Small, S. J.: Exploring the effects of hillslope-channel link dynamics and excess rainfall properties on the scaling structure of peak-discharge, *Advances in Water Resources*, 64, 9–20, <https://doi.org/10.1016/j.advwatres.2013.11.010>, 2014.
- Baltas, E. A., Dervos, N. A., and Mimikou, M. A.: Technical Note: Determination of the SCS initial abstraction ratio in an experimental watershed in Greece, *Hydrology and Earth System Sciences*, 11, 1825–1829, <https://doi.org/10.5194/hess-11-1825-2007>, 2007.
- 835 Banasik, K., Hejduk, L., Woodward, D. E., and Banasik, J.: Flood Peak Discharge vs. Various CN and Rain Duration in a Small Catchment, *Rocznik Ochrona Środowiska*, Tom 18, cz. 1, 2016.
- Blöschl, G.: *Runoff Prediction in Ungauged Basins: Synthesis Across Processes, Places and Scales*, Cambridge University Press, 491 pp., 2013.
- 840 Blöschl, G., Bierkens, M. F. P., Chambel, A., Cudenneq, C., Destouni, G., Fiori, A., Kirchner, J. W., McDonnell, J. J., Savenije, H. H. G., Sivapalan, M., Stumpp, C., Toth, E., Volpi, E., Carr, G., Lupton, C., Salinas, J., Széles, B., Viglione, A., Aksoy, H., Allen, S. T., Amin, A., Andréassian, V., Arheimer, B., Aryal, S. K., Baker, V., Bardsley, E., Barendrecht, M. H., Bartosova, A., Batelaan, O., Berghuijs, W. R., Beven, K., Blume, T., Bogaard, T., Borges de Amorim, P., Böttcher, M. E., Boulet, G., Breinl, K., Brilly, M., Brocca, L., Buytaert, W., Castellarin, A., Castelletti, A., Chen, X., Chen, Y., Chen, Y., Chiffard, P., Claps, P., Clark, M. P., Collins, A. L., Croke, B., Dathe, A., David, P. C., de Barros, F. P. J., de Rooij, G., Di Baldassarre, G., 845 Driscoll, J. M., Duethmann, D., Dwivedi, R., Eris, E., Farmer, W. H., Feiccabrino, J., Ferguson, G., Ferrari, E., Ferraris, S., Fersch, B., Finger, D., Foglia, L., Fowler, K., Gartsman, B., Gascoïn, S., Gaume, E., Gelfan, A., Geris, J., Gharari, S., Gleeson, T., Glendell, M., Gonzalez Bevacqua, A., González-Dugo, M. P., Grimaldi, S., Gupta, A. B., Guse, B., Han, D., Hannah, D., Harpold, A., Haun, S., Heal, K., Helfricht, K., Herrnegger, M., Hipsey, M., Hlaváčiková, H., Hohmann, C., Holko, L., Hopkinson, C., Hrachowitz, M., Illangasekare, T. H., Inam, A., Innocente, C., Istanbuluoglu, E., Jarihani, B., et al.: Twenty- 850 three unsolved problems in hydrology (UPH) – a community perspective, *Hydrological Sciences Journal*, 64, 1141–1158, <https://doi.org/10.1080/02626667.2019.1620507>, 2019.
- Bracken, L. J. and Croke, J.: The concept of hydrological connectivity and its contribution to understanding runoff-dominated geomorphic systems, *Hydrological Processes*, 21, 1749–1763, <https://doi.org/10.1002/hyp.6313>, 2007.
- 855 Brocca, L., Tullo, T., Melone, F., Moramarco, T., and Morbidelli, R.: Catchment scale soil moisture spatial–temporal variability, *Journal of Hydrology*, 422–423, 63–75, <https://doi.org/10.1016/j.jhydrol.2011.12.039>, 2012.
- Cantreul, V., Biielders, C., Calsamiglia, A., and Degré, A.: How pixel size affects a sediment connectivity index in central Belgium, *Earth Surface Processes and Landforms*, 43, 884–893, <https://doi.org/10.1002/esp.4295>, 2018.
- 860 Cantreul, V., Pineux, N., Swerts, G., Biielders, C., and Degré, A.: Performance of the LandSoil expert-based model to map erosion and sedimentation: application to a cultivated catchment in central Belgium, *Earth Surface Processes and Landforms*, 45, 1376–1391, <https://doi.org/10.1002/esp.4808>, 2020.



- Cho, Y., Engel, B. A., and Merwade, V. M.: A spatially distributed Clark's unit hydrograph based hybrid hydrologic model (Distributed-Clark), *Hydrological Sciences Journal*, 63, 1519–1539, <https://doi.org/10.1080/02626667.2018.1516042>, 2018.
- Chocat, B., Thibault, S., and Zimmermann, M.: Étude comparative des résultats fournis par la méthode de CAQUOT et le modèle du réservoir linéaire, *Techniques et sciences municipales, l'Eau*, 417–423, 1981.
- 865 Chow, V.: *Open channel hydraulics*, 1959.
- Chow, V. T., Maidment, D. R., and Mays, L. W.: *Applied hydrology*, McGraw-Hill, New York, 572 pp., 1988.
- Costa, F. F. da, Paz, A. R. da, and Piccilli, D. G. A.: Modified NRCS-CN-TUH methods for distributed rainfall-runoff modeling, *RBRH*, 24, e21, <https://doi.org/10.1590/2318-0331.241920180104>, 2019.
- Demarcin, P., Sohier, C., Ilah Mokadem, A., Dautrebande, S., and Degré, A.: Essai de cartographie des classes d'infiltrabilité des sols de Wallonie (Belgique), *Biotechnol. Agron. Soc. Environ.*, 2011.
- 870 Ennouini, W., Fenocchi, A., Petaccia, G., Persi, E., and Sibilla, S.: A complete methodology to assess hydraulic risk in small ungauged catchments based on HEC-RAS 2D Rain-On-Grid simulations, *Nat Hazards*, 120, 7381–7409, <https://doi.org/10.1007/s11069-024-06515-2>, 2024.
- Environment Agency: Flood and coastal erosion risk management report: 1 April 2024 to 31 March 2025, UK Government, 2025.
- 875 Erpicum, M., Nouri, M., and Demoulin, A.: The Climate of Belgium and Luxembourg, in: *Landscapes and Landforms of Belgium and Luxembourg*, edited by: Demoulin, A., Springer International Publishing, Cham, 35–41, https://doi.org/10.1007/978-3-319-58239-9_3, 2018.
- Fentie, B., Yu, B., Silburn, M. D., and Ciesiolka, C. A. A.: Evaluation of eight different methods to predict hillslope runoff rates for a grazing catchment in Australia, *Journal of Hydrology*, 261, 102–114, [https://doi.org/10.1016/S0022-1694\(02\)00017-3](https://doi.org/10.1016/S0022-1694(02)00017-3), 2002.
- 880 Gericke, O. J. and Smithers, J. C.: Review of methods used to estimate catchment response time for the purpose of peak discharge estimation, *Hydrological Sciences Journal*, 59, 1935–1971, <https://doi.org/10.1080/02626667.2013.866712>, 2014.
- Grimaldi, S., Petroselli, A., Alonso, G., and Nardi, F.: Flow time estimation with spatially variable hillslope velocity in ungauged basins, *Advances in Water Resources*, 33, 1216–1223, <https://doi.org/10.1016/j.advwatres.2010.06.003>, 2010.
- 885 Grimaldi, S., Petroselli, A., Tauro, F., and Porfiri, M.: Time of concentration: a paradox in modern hydrology, *Hydrological Sciences Journal*, 57, 217–228, <https://doi.org/10.1080/02626667.2011.644244>, 2012.
- Grimaldi, S., Petroselli, A., and Romano, N.: Green-Ampt Curve-Number mixed procedure as an empirical tool for rainfall-runoff modelling in small and ungauged basins, *Hydrological Processes*, 27, 1253–1264, <https://doi.org/10.1002/hyp.9303>, 2013.
- 890 Hawkins, R., Ward, T. J., Woodward, D., and Mullem, J. A.: *Curve Number Hydrology: State of the Practice*, 1 pp., <https://doi.org/10.1061/9780784410042>, 2008.
- Hjelmfelt, A. T.: Investigation of Curve Number Procedure, *Journal of Hydraulic Engineering*, 117, 725–737, [https://doi.org/10.1061/\(ASCE\)0733-9429\(1991\)117:6\(725\)](https://doi.org/10.1061/(ASCE)0733-9429(1991)117:6(725)), 1991.



- 895 Hrachowitz, M., Savenije, H. H. G., Blöschl, G., McDonnell, J. J., Sivapalan, M., Pomeroy, J. W., Arheimer, B., Blume, T., Clark, M. P., Ehret, U., Fenicia, F., Freer, J. E., Gelfan, A., Gupta, H. V., Hughes, D. A., Hut, R. W., Montanari, A., Pande, S., Tetzlaff, D., Troch, P. A., Uhlenbrook, S., Wagener, T., Winsemius, H. C., Woods, R. A., Zehe, E., and Cudennec, C.: A decade of Predictions in Ungauged Basins (PUB)—a review, *Hydrological Sciences Journal*, 58, 1198–1255, <https://doi.org/10.1080/02626667.2013.803183>, 2013.
- 900 Institut Royal Météorologique de Belgique (IRM): Climat de Chastre (INS 25117) – Normales climatologiques 1991–2020, Belgique, 2023.
- Istanbuluoğlu, E., Tarboton, D. G., Pack, R. T., and Luce, C.: A probabilistic approach for channel initiation, *Water Resources Research*, 38, 61–14, <https://doi.org/10.1029/2001WR000782>, 2002.
- Jain, M. K., Mishra, S. K., Suresh Babu, P., Venugopal, K., and Singh, V. P.: Enhanced Runoff Curve Number Model Incorporating Storm Duration and a Nonlinear I_a -S Relation, *Journal of Hydrologic Engineering*, 11, 631–635, [https://doi.org/10.1061/\(ASCE\)1084-0699\(2006\)11:6\(631\)](https://doi.org/10.1061/(ASCE)1084-0699(2006)11:6(631)), 2006.
- Jenson, S. K. and Domingue, J. O.: Extracting topographic structure from digital elevation data for geographic information system analysis, *Photogrammetric engineering and remote sensing*, 54, 1593–1600, 1988.
- Journée, M., Goudenhoofd, E., Vannitsem, S., and Delobbe, L.: Quantitative rainfall analysis of the 2021 mid-July flood event in Belgium, *Hydrology and Earth System Sciences*, 27, 3169–3189, <https://doi.org/10.5194/hess-27-3169-2023>, 2023.
- Kazakis, N., Kougias, I., and Patsialis, T.: Assessment of flood hazard areas at a regional scale using an index-based approach and Analytical Hierarchy Process: Application in Rhodope–Evros region, Greece, *Science of The Total Environment*, 538, 555–563, <https://doi.org/10.1016/j.scitotenv.2015.08.055>, 2015.
- Kling, H., Fuchs, M., and Paulin, M.: Runoff conditions in the upper Danube basin under an ensemble of climate change scenarios, *Journal of Hydrology*, 424–425, 264–277, <https://doi.org/10.1016/j.jhydrol.2012.01.011>, 2012.
- Kourgialas, N. N. and Karatzas, G. P.: Flood management and a GIS modelling method to assess flood-hazard areas—a case study, *Hydrological Sciences Journal*, 56, 212–225, <https://doi.org/10.1080/02626667.2011.555836>, 2011.
- Langridge, M., Gharabaghi, B., McBean, E., Bonakdari, H., and Walton, R.: Understanding the dynamic nature of Time-to-Peak in UK streams, *Journal of Hydrology*, 583, 124630, <https://doi.org/10.1016/j.jhydrol.2020.124630>, 2020.
- 920 Lidberg, W., Ågren, A., Nilsson, M., and Lundmark, T.: Evaluating pre-processing methods of digital elevation models for hydrological modelling, *Hydrological Processes*, 31, <https://doi.org/10.1002/hyp.11385>, 2017.
- Lima, D. M., da Paz, A. R., Xuan, Y., and Piccilli, D. G. A.: Incorporating spatial variability in surface runoff modeling with new DEM-based distributed approaches, *Comput Geosci*, <https://doi.org/10.1007/s10596-024-10321-x>, 2024.
- Lindsay, J. B.: Whitebox GAT: A case study in geomorphometric analysis, *Computers & Geosciences*, 95, 75–84, <https://doi.org/10.1016/j.cageo.2016.07.003>, 2016.
- 925 Macchione, F., Graziano, A. A., and Nisticò, D.: Large-Scale 2D Rain-on-Grid Hydrodynamic Mapping of Flash and Pluvial Floods with Network-Consistent Return Periods, *Water*, 18, <https://doi.org/10.3390/w18080950>, 2026.
- Maugnard, A.: Characterization and prediction of ephemeral gully erosion in Wallonia, PhD, Université Catholique de Louvain, Louvain-la-Neuve, 184 pp., 2015.



- 930 McCuen, R. H.: Uncertainty Analyses of Watershed Time Parameters, *Journal of Hydrologic Engineering*, 14, 490–498, [https://doi.org/10.1061/\(ASCE\)HE.1943-5584.0000011](https://doi.org/10.1061/(ASCE)HE.1943-5584.0000011), 2009.
- McCuen, R. H. and Spiess, J. M.: Assessment of Kinematic Wave Time of Concentration, *Journal of Hydraulic Engineering*, 121, 256–266, [https://doi.org/10.1061/\(ASCE\)0733-9429\(1995\)121:3\(256\)](https://doi.org/10.1061/(ASCE)0733-9429(1995)121:3(256)), 1995.
- 935 McCuen, R. H., Johnson, P. A., and Ragan, R. M.: HIGHWAY HYDROLOGY: HYDRAULIC DESIGN SERIES NO. 2, 1996.
- Merz, R. and Blöschl, G.: A process typology of regional floods, *Water Resources Research*, 39, <https://doi.org/10.1029/2002WR001952>, 2003.
- Meyersohn, W. D.: Runoff Prediction for Dam Safety Evaluations Based on Variable Time of Concentration, *Journal of Hydrologic Engineering*, 21, 04016031, [https://doi.org/10.1061/\(ASCE\)HE.1943-5584.0001406](https://doi.org/10.1061/(ASCE)HE.1943-5584.0001406), 2016.
- 940 Michailidi, E., Antoniadis, S., Koukouvinos, A., Bacchi, B., and Efstratiadis, A.: Timing the time of concentration: shedding light on a paradox, *Hydrological Sciences Journal*, 63, 721–740, <https://doi.org/10.1080/02626667.2018.1450985>, 2018.
- Michel, C., Andréassian, V., and Perrin, C.: Soil Conservation Service Curve Number method: How to mend a wrong soil moisture accounting procedure?, *Water Resources Research*, 41, <https://doi.org/10.1029/2004WR003191>, 2005.
- 945 Mishra, S. K. and Singh, V. P.: Soil Conservation Service Curve Number (SCS-CN) Methodology, Springer Netherlands, Dordrecht, <https://doi.org/10.1007/978-94-017-0147-1>, 2003.
- Mishra, S. K., Jain, M. K., and Singh, V. P.: Evaluation of the SCS-CN-Based Model Incorporating Antecedent Moisture, *Water Resour Manage*, 18, 567–589, <https://doi.org/10.1007/s11269-004-8765-1>, 2004.
- Mockus, V.: Watershed lag, US Dept. of Agriculture, Soil Conservation Service, ES-1015, Washington, DC, 3, 275–370, 1961.
- 950 Moghadasi, N., Karimirad, I., Sheikh, V., Moghadasi, N., Karimirad, I., and Sheikh, V.: Assessing the Impact of Land Use Changes and Rangelands and Forest Degradation on Flooding Using Watershed Modeling System, in: *Natural Hazards - Risk Assessment and Vulnerability Reduction*, IntechOpen, <https://doi.org/10.5772/intechopen.77041>, 2018.
- Moglen, G. E. and Hartman, G. L.: Resolution Effects on Hydrologic Modeling Parameters and Peak Discharge, *Journal of Hydrologic Engineering*, 6, 490–497, [https://doi.org/10.1061/\(ASCE\)1084-0699\(2001\)6:6\(490\)](https://doi.org/10.1061/(ASCE)1084-0699(2001)6:6(490)), 2001.
- 955 Montgomery, D. R. and Dietrich, W. E.: Where do channels begin?, *Nature*, 336, 232–234, <https://doi.org/10.1038/336232a0>, 1988.
- Moriasi, D., Gitau, M., Pai, N., and Daggupati, P.: *Hydrologic and Water Quality Models: Performance Measures and Evaluation Criteria*, 2015.
- 960 Mudashiru, R. B., Sabtu, N., Abustan, I., and Balogun, W.: Flood hazard mapping methods: A review, *Journal of Hydrology*, 603, 126846, <https://doi.org/10.1016/j.jhydrol.2021.126846>, 2021.
- Munawar, H. S., Hammad, A. W. A., and Waller, S. T.: Remote Sensing Methods for Flood Prediction: A Review, *Sensors*, 22, <https://doi.org/10.3390/s22030960>, 2022.



- 965 Murphy, P. N. C., Ogilvie, J., Meng, F.-R., and Arp, P.: Stream network modelling using lidar and photogrammetric digital elevation models: a comparison and field verification, *Hydrological Processes*, 22, 1747–1754, <https://doi.org/10.1002/hyp.6770>, 2008.
- Neitsch, S. L., Arnold, J. G., Kiniry, J. R., and Williams, J. R.: Soil and water assessment tool theoretical documentation version 2009, Texas Water Resources Institute, 2011.
- 970 Nejadhashemi, A. P., Sheridan, J. M., Shirmohammadi, A., and Montas, H. J.: Hydrograph Separation by Incorporating Climatological Factors: Application to Small Experimental Watersheds, *JAWRA Journal of the American Water Resources Association*, 43, 744–756, <https://doi.org/10.1111/j.1752-1688.2007.00059.x>, 2007.
- O’Callaghan, J. F. and Mark, D. M.: The extraction of drainage networks from digital elevation data, *Computer Vision, Graphics, and Image Processing*, 28, 323–344, [https://doi.org/10.1016/S0734-189X\(84\)80011-0](https://doi.org/10.1016/S0734-189X(84)80011-0), 1984.
- Ogden, F. L. and Dawdy, D. R.: Peak Discharge Scaling in Small Hortonian Watershed, *Journal of Hydrologic Engineering*, 8, 64–73, [https://doi.org/10.1061/\(ASCE\)1084-0699\(2003\)8:2\(64\)](https://doi.org/10.1061/(ASCE)1084-0699(2003)8:2(64)), 2003.
- 975 Paiva, R. and Lima, S.: A Simple Model of Flood Peak Attenuation, *Water Resources Research*, 60, <https://doi.org/10.1029/2023WR034692>, 2024.
- Panigrahi, A. and Ramadas, M.: Revisiting the Curve Number Approach for Improving Surface Runoff Estimation: A State-of-the-Art Review, *Journal of Irrigation and Drainage Engineering*, 151, 03125001, <https://doi.org/10.1061/JIDEDH.IRENG-10173>, 2025.
- 980 Papaioannou, G., Efstratiadis, A., Vasiliades, L., Loukas, A., Papalexiou, S. M., Koukouvinos, A., Tsoukalas, I., and Kossieris, P.: An operational method for Floods Directive implementation in ungauged urban areas, *Hydrology*, 5, <https://doi.org/10.3390/hydrology5020024>, 2018.
- Pineux, N., Michel, B., Legrain, X., Bielders, C. L., Degré, A., and Colinet, G.: Diachronic soil surveys: A method for quantifying long-term diffuse erosion?, *Geoderma Regional*, 10, 102–114, <https://doi.org/10.1016/j.geodrs.2017.06.001>, 2017.
- 985 Ponce, V. M. and Hawkins, R. H.: Runoff Curve Number: Has It Reached Maturity?, *Journal of Hydrologic Engineering*, 1, 11–19, [https://doi.org/10.1061/\(ASCE\)1084-0699\(1996\)1:1\(11\)](https://doi.org/10.1061/(ASCE)1084-0699(1996)1:1(11)), 1996.
- Prakash, H., Pandey, K. K., and Soni, P.: Peak discharge estimation for ungauged basins: a review, *Journal of Water and Climate Change*, 16, 3483–3507, <https://doi.org/10.2166/wcc.2025.153>, 2025.
- 990 Radoux, J., Bourdouxhe, A., Coppée, T., De Vroey, M., Dufrêne, M., and Defourny, P.: A Consistent Land Cover Map Time Series at 2 m Spatial Resolution—The LifeWatch 2006-2015-2018-2019 Dataset for Wallonia, *Data*, 8, 13, <https://doi.org/10.3390/data8010013>, 2022.
- Sahu, R. K., Mishra, S. K., and Eldho, T. I.: Improved Storm Duration and Antecedent Moisture Condition Coupled SCS-CN Concept-Based Model, *Journal of Hydrologic Engineering*, 17, 1173–1179, [https://doi.org/10.1061/\(ASCE\)HE.1943-5584.0000443](https://doi.org/10.1061/(ASCE)HE.1943-5584.0000443), 2012.
- 995 Scharffenberg, W. A. and Fleming, M.: Hydrologic Modeling System HEC-HMS—User’s Manual (ver. 4.0), USACE: Davis, CA, USA, 2013.
- Schneider, L. E. and McCuen, R. H.: Statistical Guidelines for Curve Number Generation, *Journal of Irrigation and Drainage Engineering*, 131, 282–290, [https://doi.org/10.1061/\(ASCE\)0733-9437\(2005\)131:3\(282\)](https://doi.org/10.1061/(ASCE)0733-9437(2005)131:3(282)), 2005.



- 1000 Sohier, C. and Degre, A.: Modélisation pré-normative de pratiques agricoles et agro-environnementales en vue des plans de gestion des eaux de surface et souterraines en Région wallonne à l'aide du modèle EPICgrid-Qualvados, 2011.
- Sohier, C., Degré, A., and Dautrebande, S.: From root zone modelling to regional forecasting of nitrate concentration in recharge flows - The case of the Walloon Region (Belgium), *J. Hydrol.*, 369, 350–359, <https://doi.org/10.1016/j.jhydrol.2009.02.041>, 2009.
- Soil Conservation Service (SCS): National Engineering Handbook, Section 4: Hydrology, The Service, 612 pp., 1972.
- 1005 Soulis, K. X.: Soil Conservation Service Curve Number (SCS-CN) Method: Current Applications, Remaining Challenges, and Future Perspectives, *Water*, 13, 192, <https://doi.org/10.3390/w13020192>, 2021.
- Tarolli, P.: High-resolution topography for understanding Earth surface processes: Opportunities and challenges, *Geomorphology*, 216, 295–312, <https://doi.org/10.1016/j.geomorph.2014.03.008>, 2014.
- 1010 Thomas, I. A., Jordan, P., Shine, O., Fenton, O., Mellander, P.-E., Dunlop, P., and Murphy, P. N. C.: Defining optimal DEM resolutions and point densities for modelling hydrologically sensitive areas in agricultural catchments dominated by microtopography, *International Journal of Applied Earth Observation and Geoinformation*, 54, 38–52, <https://doi.org/10.1016/j.jag.2016.08.012>, 2017.
- Torri, D. and Poesen, J.: A review of topographic threshold conditions for gully head development in different environments, *Earth-Science Reviews*, 130, 73–85, <https://doi.org/10.1016/j.earscirev.2013.12.006>, 2014.
- 1015 USDA-NRCS: Part 630 Hydrology National Engineering Handbook, USDA-NRCS (United States Department of Agriculture-Natural Resources Conservation Service), (Chapter 15) Time of Concentration, 2010.
- Van Der Knijff, J. M., Younis, J., and De Roo, A. P. J.: LISFLOOD: a GIS-based distributed model for river basin scale water balance and flood simulation, *International Journal of Geographical Information Science*, 24, 189–212, 2010.
- Van Oost, K.: Spatially distributed modelling of surface runoff, K.U. Leuven, 2003.
- 1020 Vaze, J., Teng, J., and Spencer, G.: Impact of DEM accuracy and resolution on topographic indices, *Environmental Modelling & Software*, 25, 1086–1098, <https://doi.org/10.1016/j.envsoft.2010.03.014>, 2010.
- Veeck, S., da Costa, F. F., Correia Lima, D. L., da Paz, A. R., and Allasia Piccilli, D. G.: Scale dynamics of the HIDROPIXEL high-resolution DEM-based distributed hydrologic modeling approach, *Environmental Modelling & Software*, 127, 104695, <https://doi.org/10.1016/j.envsoft.2020.104695>, 2020.
- 1025 Verma, S., Mishra, S. K., Singh, A., Singh, P. K., and Verma, R. K.: An enhanced SMA based SCS-CN inspired model for watershed runoff prediction, *Environ Earth Sci*, 76, 736, <https://doi.org/10.1007/s12665-017-7062-2>, 2017.
- Viglione, A., Chirico, G. B., Komma, J., Woods, R., Borga, M., and Blöschl, G.: Quantifying space-time dynamics of flood event types, *Journal of Hydrology*, 394, 213–229, <https://doi.org/10.1016/j.jhydrol.2010.05.041>, 2010.
- 1030 Vojtek, M., Petroselli, A., Vojteková, J., and Asgharinia, S.: Flood inundation mapping in small and ungauged basins: sensitivity analysis using the EBA4SUB and HEC-RAS modeling approach, *Hydrology Research*, 50, 1002–1019, <https://doi.org/10.2166/nh.2019.163>, 2019.



Walega, A., Amatya, D. M., Caldwell, P., Marion, D., and Panda, S.: Assessment of storm direct runoff and peak flow rates using improved SCS-CN models for selected forested watersheds in the Southeastern United States, *Journal of Hydrology: Regional Studies*, 27, 100645, <https://doi.org/10.1016/j.ejrh.2019.100645>, 2020.

1035 Wang, Z., Zhang, G., Wang, C., and Xing, S.: Gully Morphological Characteristics and Topographic Threshold Determined by UAV in a Small Watershed on the Loess Plateau, *Remote Sensing*, 14, <https://doi.org/10.3390/rs14153529>, 2022.

Williams, J. R., Nicks, A. D., and Arnold, J. G.: Simulator for Water Resources in Rural Basins, *Journal of Hydraulic Engineering*, 111, 970–986, [https://doi.org/10.1061/\(ASCE\)0733-9429\(1985\)111:6\(970\)](https://doi.org/10.1061/(ASCE)0733-9429(1985)111:6(970)), 1985.

1040 Woltemade, C. J. and Potter, K. W.: A watershed modeling analysis of fluvial geomorphologic influences on flood peak attenuation, *Water Resources Research*, 30, 1933–1942, <https://doi.org/10.1029/94WR00323>, 1994.

Woodward, D. E., Hawkins, R. H., Jiang, R., Hjelmfelt, J., Van Mullem, J. A., and Quan, Q. D.: Runoff Curve Number Method: Examination of the Initial Abstraction Ratio, 1–10, [https://doi.org/10.1061/40685\(2003\)308](https://doi.org/10.1061/40685(2003)308), 2003.